CrossMark

A Phenomenological Model for the Light Curve of Three Quiescent Low-inclination Dwarf Novae and One Pre-cataclysmic Variable

Zhibin Dai (戴智斌)[1,2,3,4,5] , Paula Szkody[6] , Mark Kennedy[7] , Jie Su (苏杰)[1,2,4] , N. Indika Medagangoda[8],
Edward L. Robinson[9], Peter M. Garnavich[10] , and L. Malith M. De Silva[11]

[1] Yunnan Observatories, Chinese Academy of Sciences, 396 Yangfangwang, Guandu District, Kunming, 650216, People's Republic of China
zhibin_dai@ynao.ac.cn
[2] Key Laboratory for the Structure and Evolution of Celestial Objects, Chinese Academy of Sciences, 396 Yangfangwang, Guandu District, Kunming, 650216, People's Republic of China
[3] Key Laboratory of Optical Astronomy, National Astronomical Observatories, Chinese Academy of Sciences, Beijing 100101, People's Republic of China
[4] Center for Astronomical Mega-Science, Chinese Academy of Sciences, 20A Datun Road, Chaoyang District, Beijing, 100012, People's Republic of China
[5] University of Chinese Academy of Sciences, No.19(A) Yuquan Road, Shijingshan District, Beijing, 100049, People's Republic of China
[6] University of Washington, Seattle, WA, 98195, USA
[7] Jodrell Bank Centre for Astrophysics, School of Physics and Astronomy, The University of Manchester, Manchester M13 9PL, UK
[8] Arthur C. Clarke Institute for Modern Technologies, Sri Lanka
[9] University of Texas at Austin, Austin, TX, USA
[10] University of Notre Dame, Notre Dame, IN, 46556, USA
[11] Sabaragamuwa University of Sri Lanka, Sri Lanka
Received 2018 May 16; revised 2018 August 15; accepted 2018 August 17; published 2018 September 12

Abstract

We used the light curve code XRBinary to model the quiescent *K2* light curves of three low-inclination cataclysmic variables (CVs): 1RXS J0632+2536 (J0632+2536), RZ Leo, TW Vir and the pre-CV WD 1144+011. Optimized light curve models were obtained using a nonlinear fitting code NMfit and visualized by Phoebe 2.0. The disk model of J0632+2536 shows that one hotspot at the edge of the disk is enough to describe its light curve, while the other two dwarf nova (DN): RZ Leo and TW Vir require two hotspots. A typical pre-CV model with a weak irradiation effect for WD 1144+011 can explain its single-hump modulation and the newly observed spectrum confirms its previous classification. The synthetic analyses for the DN clearly indicate that phase zero of the double-hump modulations occurs around the secondary minimum and the primary hump is mainly caused by the hotspot at the edge of the disk. The quiescent disk has a flat temperature distribution with a power index of ∼0.11. The disk model of RZ Leo implies a truncated disk, supporting its previously speculated classification as an intermediate polar (IP). Except for the IP model of RZ Leo, which lacks a component related to the inferred accretion curtain, the models of J0632+2536, TW Vir and WD 1144+011 are consistent with results from the *Gaia* mission. The derived masses and radii of the secondaries of the three DN are consistent with the semi-empirical relations for CV donor stars, while their effective temperatures are higher than the predictions. Irradiation of the donor stars is investigated to explain this discrepancy.

Key words: binaries (including multiple): close – novae, cataclysmic variables – white dwarfs

1. Introduction

Dwarf novae (DN) are a subtype of primarily non-magnetic cataclysmic variables (CVs), in which a white dwarf primary accretes matters from a Roche-lobe filling late-type star via the inner (L1) Lagrange point (Warner 2003). An accretion disk can extend to the white dwarf surface via viscous processes between adjacent accretion annuli (e.g., friction and shear) due to the weak magnetic field of the white dwarf in DN ($B < 10^6$ G). Systems in which the magnetic field of the white dwarf is large enough ($10^6 < B \leqslant 10^7$ G) for the accretion disk to be disrupted inside the white dwarf magnetosphere and for material to begin to follow the magnetic field lines are called Intermediate Polars (IPs). In the following, we assume that the disk outside of the magnetosphere in an IP is equivalent in structure to the disk in a regular non-magnetic DN. The interaction between the ballistic stream leaving the L1 point and the accretion disk forms a region of energy release at the edge of the disk, which is called a hotspot. The combination of an accretion disk and a hotspot (hereafter just called the disk model) has been used as the typical accretion model for CVs (e.g., Smak 1970; Warner 2003) and has been quite successful in describing the asymmetrical eclipse profile of several high-inclination CVs during quiescence (e.g.,

Wood & Crawford 1986; Bruch 1996). This model can also be used to explain a symmetrical CV eclipse profiles during outburst (e.g., Kato et al. 2003; Bąkowska & Olech 2015), which is caused by the significant flux increase of the disk (i.e., the luminous accretion disk almost overwhelms the relatively faint white dwarf and hotspot).

Several high-inclination CVs in quiescence have been comprehensively studied using this disk model (e.g., Cook & Waner 1984; Bailey & Cropper 1991; McAllister et al. 2015). By detecting variations in the mid-eclipse times, substellar objects have been suggested to exist in several DN (e.g., V2051 Oph, Qian et al. 2015; and EM Cyg, Dai & Qian 2010a). In addition, many synthetic light curve analysis methods (e.g., BINSYN program, Linnell et al. 2012; Eclipsing Light Curve Code, Orosz & Hauschildt 2000; and the cool-disk model, Khruzina 2011) have been developed to analyze CV eclipse light curves. The irregular eclipse light curves of quiescent CVs are composed of the occultations of multiple components, including the white dwarf, the accretion disk and hotspots (e.g., Smak 1994; Feline et al. 2004; Littlefair et al. 2014; McAllister et al. 2015). High-inclination CVs only show a single eclipse in one orbit (i.e., the secondary eclipse of the red dwarf is

invisible; e.g., Krzeminski 1965; Bailey et al. 1988) because the red dwarf in a CV system is usually regarded to be a very faint component compared with the accretion disk and the white dwarf. This *single-eclipse* feature implies that CV eclipse light curves cannot reveal full information about the red dwarf companion. Due to the complexity of the quiescent CV eclipse light curves, high time resolution is necessary to decompose all components. However, over 70% of CVs with short orbital periods (<3 hr) are fainter than 17 mag in quiescence based on the updated CV catalog (RKcat Edition 7.24, which was first published in Ritter & Kolb 2003). Therefore, the majority of CVs have only low time-resolution photometry comprised of blended flux from many components, which makes modeling these systems difficult. For example, recent discussions concerning two new-found CVs with deep eclipses carried out by Kjurkchieva et al. (2015) and Kennedy et al. (2016) have clearly indicated that the model light curves cannot perfectly fit the observed eclipsing light curves during ingress and outside of eclipse. Assuming that a deep eclipse is a common feature of CVs with orbital inclination higher than 80°, the fraction of low-inclination CVs can be simply estimated to be around 90%. To determine a general model independent of inclination, it is necessary to consider low-inclination CVs.

The unprecedented light curves from the *Kepler K2* mission (Howell et al. 2014), with nearly continuous photometric coverage for 1–3 months at different pointings (Campaigns) along the ecliptic provide an excellent database to study quiescent CV light curves. *K2* Campaign 0 (K2-C0) was an engineering test in the early stage of the *K2* program and only covered ~35 days because the spacecraft was not in fine point during the beginning of the campaign, while *K2* Campaign 1 (K2-C1) covered a complete period of 80 days. In this paper, we focus on the phased light curves of four systems: 1RXS J0632+2536 (hereafter J0632+2536) and TW Vir, which are both DNs; RZ Leo, which is an unusual IP that also has displayed DN outbursts, making it one of the few systems to be both a magnetic system and a DN; and WD 1144 +011, which is a pre-CV (meaning that the secondary is probably not filling its Roche lobe). J0632+2536 was observed in K2-C0, while TW Vir, RZ Leo and WD 1144+011 were observed in K2-C1. The phased light curves are investigated in detail using the synthesis methods XRBinary and NMfit described in Section 3. Due to the lack of any eclipse feature, all four objects are likely low-inclination systems. The preset model parameters are discussed in Sections 4 and 5. The details of the white dwarf accretion structure during quiescence and the physical parameters of the stars in each system are further discussed and visualized in Section 6.

2. Phased Light Curves

Dai et al. (2016) used the PyKE suite of software tools developed by the Guest Observer Office (Still & Barclay 2012) to extract the *K2* light curves of J0632+2536, RZ Leo and WD 1144+011, and derive their orbital periods using traditional period finding techniques (e.g., Lomb–Scargle periodogram, Lomb 1976; Scargle 1982; and phase dispersion minimization, Stellingwerf 1978) and their corresponding phased light curves. Due to the unstable orbital modulations of TW Vir, Dai et al. (2017) applied a phase-correcting method to obtain its orbital period and the phased data from the quiescent data.

Based on the continuous *K2* data, we attempted to model the mean orbital light curves of each system by using an XRBinary

light curve synthesis code that was developed by E. L. Robinson.[12] The default phase zero of a light curve generated by XRBinary is an inferior conjunction of the Roche-lobe filling secondary (i.e., the accretion disk around the white dwarf is occulted by the red component), which is in accord with the phases specified in eclipsing CVs. Compared with the typical CV eclipse light curve with a narrow and deep white dwarf eclipse (e.g., Littlefair et al. 2014; McAllister et al. 2015), all four light curves derived by Dai et al. (2016, 2017) only show wide and shallow modulations with an amplitude of several hundredths up to tenths of a magnitude. Note that the phases of the obtained light curves are arbitrary. The three DN (J0632+2536, RZ Leo and TW Vir) light curves clearly show double-hump modulations, with a nearly constant phase difference of ~0.5 between the two minima dips. This means that the light minima at the lower (primary dip) and higher (secondary dip) flux levels are at phases 0.5 or zero, respectively. In principle, an irradiation effect is significant in CV systems and commonly results in a higher flux level at the phase 0.5 dip than at phase zero. However, phase zero of the double-hump modulation cannot be simply identified from this flux difference due to possible changes caused by hotspots on the disk. Therefore, for each DN with a double-hump modulation discussed in this paper, two phased light curves corresponding to phase zero at the primary and secondary dips, respectively, were analyzed to search for a final convergent solution. Since the secondary dip in TW Vir cannot be accurately measured due to large scatter in the data, the primary maximum was set to be at the reference phases 0.75 and 0.25, guaranteeing that minima would occur around phases 0.5 and zero. For the pre-CV WD 1144+011, phase zero was set to be the minimum of the light curve since the light curve shows a single-hump modulation.

The four *K2* light curves are expressed in Simple Aperture Photometry flux (i.e., electrons per second), while the light curves calculated by XRBinary are given in ergs per second. Hence, the *K2* light curves were normalized before the calculations of XRBinary. Since the huge number of data points in the observed light curves (i.e., the number of data points in the *K2* light curves observed in long cadence (LC; 30 minutes sampling) and in short cadence (SC; 1 minutes sampling) are more than 10^3 and 10^5, respectively) can take a long calculation time with XRBinary, the *K2* phased light curves are moderately binned with a uniform phase resolution 0.01. Dai et al. (2017) demonstrated that the orbital modulations of the three CVs are stable, and the large-amplitude dispersion of ~0.43 mag in the phased light curve of RZ Leo (Figure 5 of Dai et al. 2016) is only caused by a uniform drift of the system light. Thus, while the phased light curve of TW Vir has the highest stability (Dai et al. 2017), all four binned and normalized *K2* light curves represent their orbital modulations.

3. Synthesis Methods for the Light Curves

Although the XRBinary program was initially designed to calculate the light curves of low-mass X-ray binary stars (LMXBs) (Gomez et al. 2015), it can also be used to model low-inclination CVs based on the following two reasons. First, XRBinary sets the primary star as a much smaller sphere than all other dimensions in the binary system and is unresolved by any of the grids used in calculating the light curves. Like the

---

neutron star in LMXBs, the white dwarf in both CVs and pre-CVs is very small compared with the companion red dwarf. Second, XRBinary simply assumes that the primary star only emits black body radiation. This is a reasonable assumption for low-inclination CVs and pre-CVs because the flux contribution from the visible white dwarf is approximately constant. XRBinary may not be appropriate to accurately model complicated eclipse light curves but it should be able to reproduce low-inclination CV light curves. In fact, XRBinary is a powerful tool to analyze the accretion disk around the central compact star by constructing a complex accretion disk model consisting of a disk, a disk rim, a disk torus and an inner disk. Ratti et al. (2013) have successfully applied XRBinary to reproduce an ellipsoidal light curve of the CV CXOGBS J174444.7-260330 in a low state.

In this paper, a standard CV model (i.e., a semi-detached close binary system with a Roche-lobe filling red dwarf and, in the case of the 3 DN, an accretion disk around the white dwarf) with a set of geometric and physical parameters is applied to model the phased light curves of four low-inclination systems. Based on a complete set of preset parameters, XRBinary calculates a theoretical light curve and a relative measurement of goodness of fit, χ^2 (i.e., the variance between the calculated and observed light curves). Taking advantage of the improved Nelder–Mead method (i.e., Multi-directional Search method (MDS), Nelder & Mead 1965; Torczon 1989; Geng 2008), which was successfully applied to fit the O-Cs of AM Her (Dai et al. 2013) and UZ For (Dai et al. 2010b), we developed a new program called NMfit to carry out a search for the best binary model within a given parameter space. After obtaining the best binary model, NMfit sets a series of small deviations around each of the parameters to test the variations in χ^2 caused by these deviations. Note that when an adjustable parameter is intentionally set to deviate from its optimal value, then the other parameters are fixed. Moreover, this optimization method ignores degeneracies between parameters, which is a big issue. Since the best binary model means the minimal χ^2, the deviations give rise to an increase of χ^2. When χ^2 increases to 5% larger than the minimal value, this tested parameter deviation is arbitrarily regarded as the uncertainty. All of the adjustable parameters are tested one-by-one to estimate their errors. The error estimates based on χ^2 are only lower limits to the true uncertainties in the derived parameters and the true uncertainties could be quite large because the physics of compact binaries is much more complicated and XRBinary arbitrarily makes many tacit assumptions (e.g., the disk is modeled as an object with sharp, well-defined edges and surfaces, and the disk surface elements emit and absorb like black bodies). The uniform design proposed by Fang (1980) is used to decide the initial parameter set before the search iterates. A good initial parameter set is crucial for the success of the iterations. In addition, since Phoebe[13] is able to calculate and plot an accretion disk around a compact star (Prša et al. 2016), it was used to visualize the system configuration based on the best-fitting parameters derived by NMfit and XRBinary.

4. Model Parameters Preset in XRBinary

The 23 model parameters that were used to generate the light curves are listed in Table 1, which are divided up into seven

---

[13] The version of Phoebe used for the CV plotting is 2.0a2.

Table 1
All Parameters Used to Calculate Light Curves by Using XRBinary

Parameters	Values	Statements
Fixed		
STAR2TILES	5000	tiles covering star surface
DISKTILES	20,000	tiles covering disk surface
BANDPASS (Å)	$4200 \sim 9000$	bandpass of $K2$ light curve
H_{pow}	1.1	power index of H_{disk}
L_{wd}	...	white dwarf luminosity
T_{wd}	...	white dwarf temperature
R_{in}[a]	...	inner radius of disk
Adjustable		
Components		
q_{orb}	...	mass ratio
i_{orb}	...	orbital inclination
M_{wd}	...	white dwarf mass
T_{rd}	...	red dwarf temperature
R_{out}	...	outer radius of disk
H_{edge}	...	H_{disk} at the outer edge
ξ	...	power index of T_{disk}
L_{d0}	...	disk luminosity
Hotspot at the edge of disk		
T_{es}	...	temperature
ζ_{esmid}	...	centering phase
$\zeta_{eswidth}$	...	full width
Hotspot on the surface of disk		
ζ_{ssmin}	...	lower limit of boundary in ζ direction
ζ_{ssmax}	...	upper limit of boundary in ζ direction
R_{ssmin}	...	lower limit of boundary in radius direction
R_{ssmax}	...	upper limit of boundary in radius direction
T_{ratio}^{ss}	...	fractional change in T_{disk}

Note.
[a] R_{in} can be adjustable for IPs due to the disrupted inner disk.

fixed parameters and 16 adjustable parameters. Our assumptions for these parameters are as follows.

1. Although the input and output light curves of XRBinary are normalized, the typical luminosity of the white dwarf can provide an important reference for the system luminosity of the output CV model. Since the mass range for isolated white dwarfs is $0.3\,M_\odot$ to $1.4\,M_\odot$ and over 30% of white dwarfs are centered on $\sim0.56\,M_\odot$ (Berg et al. 1992; Provencal et al. 1998), the white dwarf masses of all four objects were searched in this mass range. By using the relation $L_{wd} = 4\pi R_{wd}^2\,\sigma T_{wd}^4$, the white dwarf radius R_{wd} is solely dependent on the white dwarf luminosity L_{wd} and temperature T_{wd}. According to the white dwarf mass–radius relationship, as shown in Figure 1 (e.g., Wood & Horne 1990; Provencal et al. 1998), L_{wd} can only be determined by T_{wd} for a given M_{wd}. During the iterations of NMfit, T_{wd} calculated from the adjustable parameter L_{wd} is preset to be a fixed parameter.

2. To improve the reliability of the model, a simple disk with minimal free parameters consisting of up to two hotspots (one at the vertical side of the edge of the disk (es) and the other one on the surface of the disk (ss)) is
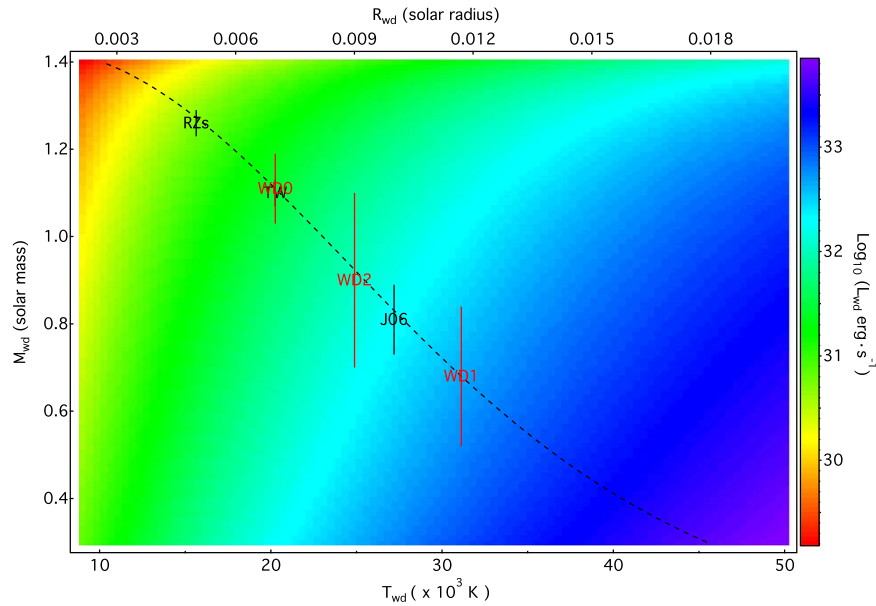
Figure 1. Colormap of the luminosity of the primary white dwarf corresponding to M_{wd} and T_{wd}. The dash line represents the typical mass–radius relationship of the white dwarf. The data point marked by RZs refer to the model of RZ Leo derived from the light curve with the phase zero at the secondary dip. The three data points marked in red by WD0, WD1 and WD2 refer to the models of WD 1144+011 by using the revised model-0, model-1 and model-2, respectively. The left two data points marked by TW and J06 refer to the models of TW Vir and J0632+2536, respectively.

used to describe the low-inclination CV light curves. This CV quiescent disk was assumed to normally extend to the surface of the white dwarf (i.e., $R_{in} = R_{wd}$). A boundary layer was not considered because it dominates the flux at ultraviolet wavelengths rather than at optical wavelengths. A hotspot on the vertical side of the edge of the disk can be completely described by three parameters: a uniform temperature T_{es}, the centering phase ζ_{esmid} and the full width $\zeta_{eswidth}$. Considering that the other hotspot on the disk surface can be visible and modulate the light curves of low-inclination CVs, this hotspot is described using five parameters: ζ_{ssmin}, ζ_{ssmax}, R_{ssmin}, R_{ssmax} and T_{ratio}. The first four parameters are the boundaries of the hotspot, which are the angles and radii over which the hotspot extends, respectively. The last parameter T_{ratio} is a fractional change in T_{disk} (i.e., $T_{ratio} = T_{ss}/T_{disk}$).

3. A different temperature distribution may exist in different quiescent accretion disks. The temperature distribution is assumed to be a power law in disk radius R_{disk}; i.e., $T_{disk} \propto R_{disk}^{\xi}$. For a steady-state disk, typically $\xi = -0.75$ (Wade & Hubeny 1998). However, subsequent papers suggested that accretion disks in CVs have much flatter temperature profiles with $\xi > -0.75$ (e.g., Marsh 1999; Orosz & Wade 2003). According to the disk instability model (Osaki & Kato 2013a, 2013b, 2014), the quiescent DN disk is an optically thin and cool disk with a flat radial temperature profile. Observations of various quiescent DN (e.g., Z Cha, Wood & Crawford 1986; OY Car, Wood et al. 1989; V2051 Oph, Rutkowski et al. 2016) confirm that their disk temperature distributions are much flatter than the prediction of $T_{disk} \propto R_{disk}^{-0.75}$. We initially assume $\xi = -0.15$ but allow this value to be adjusted by NMfit.

4. The adjustable parameter L_{d0} indicating the disk luminosity is only calculated from the temperature distribution of the disk. This parameter should satisfy a default condition that the temperature at the inner edge of disk (i.e., T_{in}) cannot be much larger than 10^4 K because the average temperature of observed quiescent disks is below 10^4 K, which is consistent with the typical temperature range of an accretion disk (from several 10^3 to 10^4 K) predicted by the limit-cycle oscillation between hot and cold states (Lasota 2001).

5. Since both theories and observations suggest that the accretion disk around a white dwarf is geometrically thin (e.g., Pringle 1991; Frank et al. 1992; Wade & Hubeny 1998; Marsh 1999), the height of the disk, H_{disk}, is assumed to obey a power low with a power index $H_{pow} = 1.1$ for all four objects, but H_{edge} is set to be adjustable.

6. Since the components of the model calculated in XRBinary (e.g., two component stars, the disk and hotspots on the disk) are independent, we can freely construct the necessary components to model the observed light curves. Three types of models, as listed in Table 2, were attempted to verify the necessity of a disk around the white dwarf and the hotspots on the disk. Model-0 is a detached binary model without a disk. Model-1 contains an accretion disk with a hotspot at the edge of the disk. Model-2 adds a second hotspot on the disk surface. The relative flux contributions in percentage from the different model components to the synthetic light curves calculated by XRBinary are shown in Figure 2. Their zero points are listed in Table 3.

5. Irradiation Effect Calculated in NMfit

The irradiation effect is only calculated by XRBinary when setting the parameter IRRADIATION to ON. Since a luminous secondary may weaken the illumination from the vicinity of the white dwarf and the disk, the parameter IRRADIATION is preset to OFF if the summation of the luminosity of the white

Table 2
The Models Used in XRBinary

Component[a]	Model-0	Model-1	Model-2
White dwarf	1	1	1
Red dwarf	1	1	1
Accretion disk	0	1	1
Hotspot on the disk surface	0	0	1

Note.
[a] The component included in the model or not is indicated by "1" or "0," respectively.

dwarf and the disk (i.e., $L_{wd}+L_d$) is smaller than the luminosity of the secondary L_{rd}. Although XRBinary can calculate the heating effect due to the irradiation, the output parameter T_{rd} of XRBinary is simply derived from L_{rd} by using the formula $L_{rd} \sim 4\pi R_{rd}^2 \sigma T_{rd}^4$. This means that T_{rd} represents the temperature of the secondary averaged over its entire surface, which can be significantly higher than the true night side temperature of the secondary if irradiation in the systems is significant. Here, the night side is the surface of the secondary facing away from the WD and disk, and the day side is the surface facing the WD and disk.

Davey & Smith (1992) found that the size of the irradiation region is usually as large as the entire day side surface of the secondary star. The numerical work by Kirbiyik (1982) suggested that the difference in the effective temperature between the day and night sides of the secondary is very large. Considering that the typical difference may reach close to 10^4 K (Warner 2003), irradiation would be easily observed if this tremendous disparity of the effective temperature exists. Therefore, an estimation of the size of the irradiation region on the surface of the secondary can help to understand the flux contribution from the irradiation region in both CV and pre-CV systems. The effective temperature of the secondary on the night side can be specified by the semi-empirical CV donor sequence (Knigge 2006; Knigge et al. 2011). The derived T_{rd} can be regarded as a lower limit to the effective temperature of the irradiation region.

Due to orbital rotation, our viewing angle of the irradiated region can change with the orbital phase. Assuming that the irradiation region on the leading side of the star[14] is axisymmetric with the line between the center points of two component stars, the flux ratio should reach a maximum between phases 0.5 and 0.0; i.e., $F_{irr} = f_{0.5}/f_{0.0}$, where $f_{0.5}$ and $f_{0.0}$ are the irradiation flux at phases 0.5 and 0.0, respectively. The details of the calculations of F_{irr} are described in Appendix A. By investigating the variations in F_{irr} along with a normalized area of the irradiation region (i.e., $S_{irr} = A_{irr}/A_{star}$, where A_{irr} and A_{star} are the areas of the irradiation region and the whole star, respectively), a relation between F_{irr} and S_{irr} based on the physical model derived by XRBinary and NMfit can be estimated and used to compare with the observed flux ratio F_{obs} between phases 0.5 and 0.0.

6. Comparisons with *Gaia* Results

Since the *K2* light curves of the four binary systems are from the broad bandpass listed in Table 1, their *K2* magnitudes

(hereafter Kp_2) translated by Dai et al. (2016) are commonly different from their apparent visual magnitudes. Assuming this magnitude difference to be a systematic error, the calculated magnitudes of the four systems (hereafter CKp_2) based on the luminosities of the models can be set to be a reference parameter for the comparisons with the results from the *Gaia* mission (Gaia Collaboration et al. 2016). Table 4 lists the distances of all four systems based on the absolute stellar parallax in the *Gaia* database (Gaia Collaboration et al. 2018).[15] CKp_2 can be estimated from the *Gaia* distance D_g derived from the *Gaia* parallax (Luri et al. 2018) and the system luminosity L_{all}, which is summed for all model components and corresponds to the zero point of the normalized *K2* light curves, by using the following formula,

$$CKp_2 = 2.5 \log\left[\frac{L_{bol0}}{L_{all}}\right] - BC_v + 5 \log\left[\frac{D_g}{10 \text{ pc}}\right], \quad (1)$$

where $L_{bol0} = 3.0128 \times 10^{35}$ erg s^{-1},[16] and BC_v is a bolometric correction of the main sequence star in the typical Johnson-Cousins V band with the solar $\log g$, [Fe/H] and [α/Fe]. Note that BC_v corresponding to the derived T_{rd} can cause an uncertainty of CKp_2 for CV and pre-CV systems because BC_v is improperly used for the white dwarf and disk. This calculated uncertainty may explain the discrepancy between CKp_2 and Kp_2.

Considering that BC_v is a model-dependent quantity with many observational constraints, several numerous tabulations are provided in the literature. All three popular BC_v tables, respectively, proposed by Flower (1996), Bessell et al. (1998) and Casagrande & VandenBerg (2014) were used to calculate CKp_2 to minimize our errors. The relations of BC_v and T_{eff} plotted in Figure 3 clearly show that the three BC_v tabulations significantly differ for cool stars with $T_{eff} \leqslant 4000$ K. Inspection of Figure 3 indicates that BC_v of RZ Leo, TW Vir and WD 1144+011 are obviously different for each table. Consequently, the difference between the three BC_v tabulations for the same T_{eff} is regarded as the uncertainty of BC_v. Compared with the two early BC_v tables of Flower (1996) and Bessell et al. (1998), the updated BC_v given by Casagrande & VandenBerg (2014) is moderate for cool stars. Therefore, they were used to calculate CKp_2 for all four systems to compare with the *K2* magnitudes at the zero point of the normalized *K2* light curves (Dai et al. 2016). The interpolated BC_v and the errors used to calculate CKp_2 for all four systems are listed in Table 4.

7. Modeling Results and Discussions

7.1. J0632+2536

This is a poorly studied DN that experienced several DN outbursts in 2009 and 2012 (Korotkiy & Sokolovsky 2012; Masi 2012; Ohshima 2012). Dai et al. (2016) showed its double-hump light curve extracted from the *K2* data archive and several quiescent spectra with strong double peaked Balmer emission lines obtained from the Large Binocular Telescope (LBT). Based on these spectra and the phased *K2* light curve, the secondary of J0632+2536 is thought to be a K5V star and the orbital inclination cannot be lower than 50°. According to the MK

---

[14] The secondary is assumed to be spherical to simplify the calculations of the irradiation effect.

[15] https://gea.esac.esa.int/archive/documentation/GDR2/Miscellaneous/sec_credit_and_citation_instructions/

[16] A zero point luminosity corresponds to an absolute bolometric magnitude scale (i.e., $M_{bol} = 0$) recommended by the IAU 2015 Resolution B2.
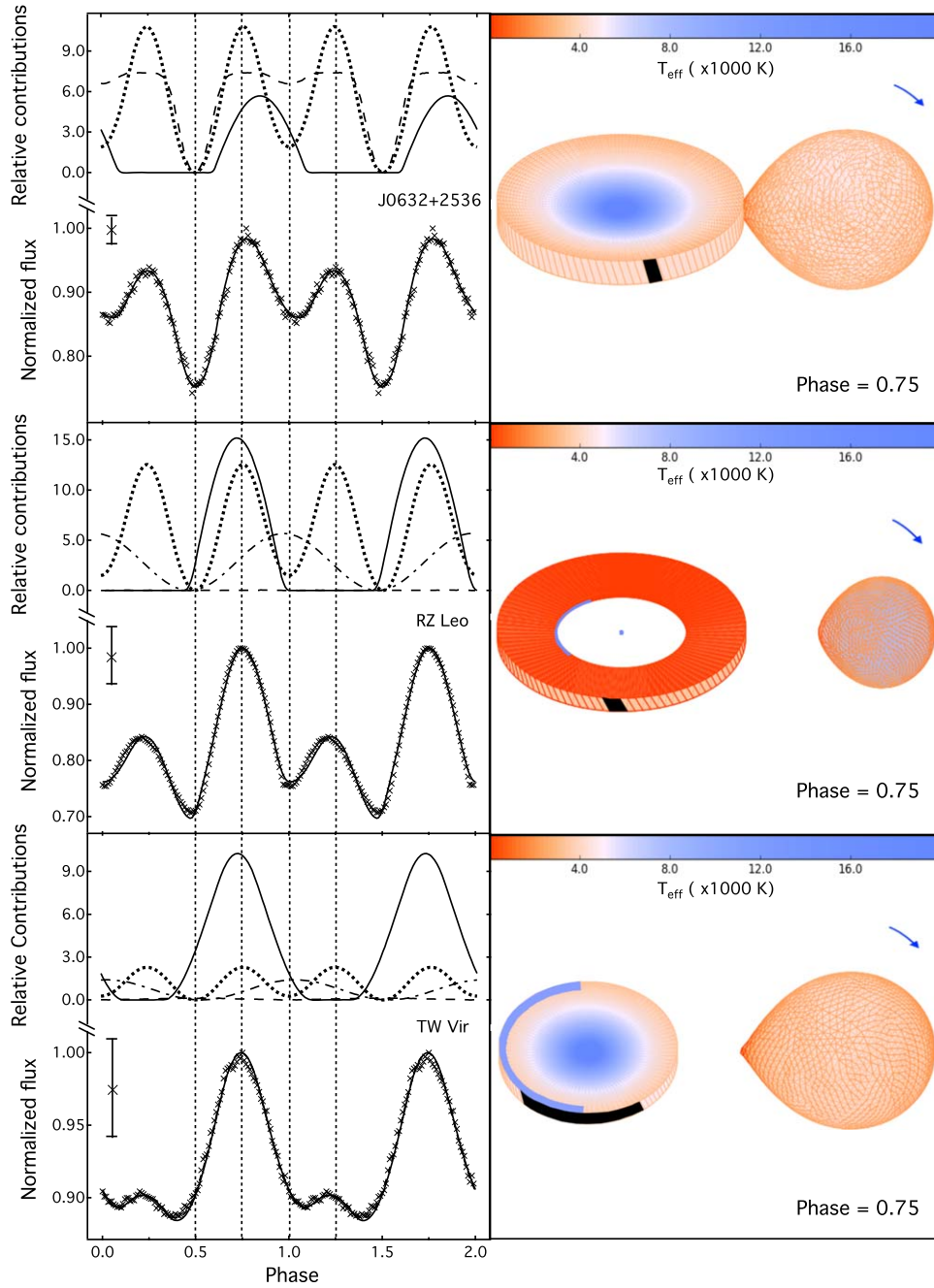
Figure 2. The phased and binned light curves of J0632+2536, RZ Leo and TW Vir superimposed with their best-fitting light curves are plotted in the three left-hand panels from top to bottom, respectively. The fluxes of all of the light curves are normalized. The relative flux contributions from different model component for three systems are plotted in percentages. The dotted and dashed lines refer to the contributions from two stellar components (white dwarf and red dwarf) and the accretion disk, respectively. The solid and dash dot lines denote the contributions from the hotspots at the edge of the disk and on the surface of the disk, respectively. They indicate what component is actually contributing to the actual light curve. The three right-hand panels show their corresponding 2D binary configurations at phase 0.75 by using the Phoebe 2.0. The color denotes the effective temperature. To visualize the hotspot at the edge of the disk, they are filled with black rather than the color picked from the color bar because the small temperature difference between the hotspot and the neighboring region of the disk can seriously reduce the contrast of the hotspot. The arrow denotes a clockwise rotation direction of the binary system.

spectral classes (Cox 2000), the initial temperature and mass of the secondary are set to be 4410 K and $0.67\,M_\odot$, respectively. Several high-precision measurements of white dwarf masses in CVs (Knigge 2006; Knigge et al. 2011; Zorotovic et al. 2011) have indicated that the mean CV white dwarf mass is usually larger than that of isolated white dwarfs (Berg et al. 1992; Kepler et al. 2007). Thus, for J0632+2536, which lacks an accurate measurement of the white dwarf mass, a mean CV white dwarf mass of $0.83\,M_\odot$ was preset to be the initial parameter

(i.e., $M_{\rm wd} = 0.83\,M_\odot$). Finally, Urban & Sion (2006) used *IUE* spectra of 53 quiescent DN to show that the temperature of a white dwarf, $T_{\rm wd}$, in a CV with an orbital period above the period gap is approximately 25,793 K (Sion 1999; Urban & Sion 2006). We assume this value for the temperature of the white dwarf in J0632+2536 because its orbital period of 0.314478 day (Dai et al. 2016) is above the gap.

A large number of trials calculated using XRBinary and NMfit suggest that a convergent solution using a normal CV

Table 3
The Zero Points of the Relative Flux Contributions from Different Component

Components[a]	J0632+2536	RZ Leo	TW Vir	WD 1144+011
Binary[b]	65.1	66.5	20.4	94.3
Starspot[c]	⋯	⋯	⋯	1.1
Disk[d]	11.7	0.0	63.0	⋯
Hotspot[es]	0.0	0.0	0.0	⋯
Hotspot[ss]	⋯	2.6	3.4	⋯

Notes.
[a] The relative flux contributions are in percentage.
[b] Only consist of white dwarf and red dwarf.
[c] Starspots on the red dwarf.
[d] Accretion disk without hotspot.

configuration cannot be achieved when setting phase zero to the primary dip of the light curve. Hence, phase zero was set for the secondary dip. Model-1 was used to model the phased light curve of J0632+2536. At first, four parameters (M_{wd}, T_{wd}, mass ratio q_{orb} and T_{rd}) were fixed and the other nine parameters consisting of the orbital inclination i_{orb} and eight parameters of the accretion disk were set to be adjustable. By using NMfit, a preliminary accretion disk model indicated that the inner radius of the disk is basically close to the white dwarf radius, so we then fixed the parameters ξ and R_{in} to derive the uncertainties of the other 11 parameters. Since ξ is an insensitive parameter, its uncertainty cannot be obtained. By using Phoebe 2.0, a 2D CV configuration at phase 0.75 shown in Figure 2 visually indicates that J0632+2536 has a large and thick accretion disk with a small hotspot at the edge of the disk. Since the orbital inclination of J0632+2536 is not high enough for the white dwarf to be occulted by the secondary, the flux contribution from the white dwarf is constant and does not vary with the orbital period, so this constant flux contribution is simply added to the ellipsoidal modulations caused by the secondary. Compared with the small white dwarf, the top panel of Figure 2 clearly shows that the large and thick accretion disk can be partially eclipsed around phase zero. Moreover, the hotspot at the edge of the disk, which has a temperature of 6200 (±100) K and has a phase width of 0.033(2) at phase 0.844(2), only contributes a maximum of 5% of the flux from the whole system. Since CKp_2 of J0632+2536 listed in Table 4 is almost equal to the corresponding Kp_2, the obtained physical model of J0632+2536 is compatible with the *Gaia* distance. However, the T_{eff} of J0632+2536 shown in the *Gaia* database is obviously higher than that derived from the LBT spectra (Dai et al. 2016) and the derived T_{rd} listed in Table 5.

The region where the mass transfer stream intersects the accretion disk (i.e., the hotspot at the edge of the disk) is simply assumed to be a rectangle with a uniform temperature T_{es} by XRBinary. A mass transfer rate $\dot{M}_{rd}$ (hereafter, the parameters with the subscript rd related to the secondary star) can be roughly estimated by using the following formula,

$$\dot{M}_{rd} \simeq \frac{L_{acc} R_{out}}{G M_{wd}}, \qquad (2)$$

where L_{acc} is the luminosity of the hotspot at the edge of the disk. The mass transfer rate can be estimated to be $\dot{M}_{rd} \sim 2.5(\pm 0.2) \times 10^{-10} M_\odot$ yr^{-1}, corresponding to a mass loss timescale (i.e., $\tau_{\dot{M}} \sim M_{rd}/\dot{M}_{rd}$) of 2.8×10^9 year. The top right-hand panel of Figure 4 indicates that $M_{rd} = 0.7(1) M_\odot$ is

closer to the semi-empirical mass-period relation of Warner (2003) than that of Smith & Dhillon (1998). Furthermore, the secondary radius $R_{rd} = 0.81$ is consistent with the radius-period relations shown in the bottom right-hand panel of Figure 4. The thermal (or Kelvin–Helmholtz) timescale of the secondary (i.e., $\tau_{kh} \sim GM_{rd}^2/(L_{rd}R_{rd})$) can be calculated to be 7.6×10^7 year, as listed in Table 6, which is smaller than the derived $\tau_{\dot{M}}$. This means that the mass transfer via the L1 point is slow and the secondary is always able to maintain thermal equilibrium. Therefore, the secondary of J0632+2536 is almost indistinguishable from an isolated main sequence star of the same mass. The derived mass and radius shown in the bottom left-hand panel of Figure 4 confirm that the secondary of J0632+2536 is a typical K5V star (Dai et al. 2016). Inspection of the top panel of Figure 2 indicates that the ellipsoidal modulations of this K5 star dominate the observed double-hump modulations. Although the top left-hand panel of Figure 4 indicates that $T_{rd} = 4540(80)$ K is nearly consistent with a normal K5V star based on the MK spectral classes (Cox 2000), this derived T_{rd} is around 350 K higher than the prediction of the semi-empirical CV donor sequence (Knigge 2006; Knigge et al. 2011). The most likely explanation for this discrepancy may be due to irradiation of the K5V star. Since the irradiation effect is not calculated by XRBinary as $L_{rd} > L_{wd} + L_d$, we investigated its strength in more detail. Based on our best-fitting model, the maximal F_{irr} is around 1.08, as shown in Figure 5. As long as 20% of the irradiation region can be occulted by the disk at phase 0.5, the observed flux ratio of J0632+2536 (i.e., $F_{obs} \sim 0.87$) can be explained. Due to our derived large disk and moderate orbital inclination, a partial eclipse of the irradiation region at phase 0.5 can be expected.

7.2. RZ Leo

Dai et al. (2016) confirmed that RZ Leo is a short-period DN with an orbital period of 0.07603 day, similar to that derived by Patterson et al. (2003) and Kato et al. (2009). Ishioka et al. (2001) and Mennickent et al. (1999) indicated that the secondary of RZ Leo should be a normal red dwarf, possibly a main sequence M0 star. Although this spectral type cannot be supported by the mass ratio of 0.14 derived from its superhump excess of 0.033 (Ishioka et al. 2001), we speculated that RZ Leo should consist of a massive white dwarf and a normal red dwarf with a small mass of $<0.2 M_\odot$. Thus, we assumed that the initial M_{rd} used in NMfit is $0.15 M_\odot$, which means $M_{wd} = 1.1 M_\odot$ and $T_{rd} \sim 3500$ K. Szkody et al. (2017) and Dai et al. (2016) detected a short white dwarf spin period of $\sim$220 s classifying RZ Leo as a member of the IP subtype of CVs. From an Ultraviolet (UV) study, Pala et al. (2017) determined that the white dwarf had a temperature of 15,014 (±638) K and contributed 83% of the UV flux. Since the humps of the model-1 light curve are located exactly at phases 0.25/0.75, model-2 with an extra hotspot on the surface of disk can be used to describe the offset secondary hump of RZ Leo. For the phased light curve with phase zero at the primary minimum, a convergent solution was found. However, inspection of the bottom left-hand panel of Figure 4 shows that the derived secondary mass and radius obviously deviate from the predicted mass–radius relation of the semi-empirical CV donor sequence (Knigge 2006; Knigge et al. 2011). Based

Table 4
The Results of Four Systems Estimated From the *Gaia* Database

Name	$T_{\rm eff}$	Parallax	D_g	$L_{\rm all}$	BC$_v$[a]	CKp$_2$[b]	Kp$_2$[c]
	K	mas	pc	$\times 10^{32}$ erg s^{-1}		mag	mag
J0632+2536	5255.5	2.24(5)	446($\pm$10)	13.2	-0.53(4)	14.67(7)	14.4
RZ Leo	$\cdots$	3.6(3)	278($\pm$23)	0.2	-1.4(4)	19.1(4)	17.6
TW Vir	4850	2.3(1)	435($\pm$19)	5.8	-1.1(1)	16.0(2)	15.9
WD1144+011	3657.5	4.7(1)	213($\pm$5)	4.8	-1.8(7)	15.5(7)	16.0

Notes.
[a] Interpolated bolometric corrections based on BC$_v$ tabulations by Casagrande & VandenBerg (2014).
[b] Calculated *K2* magnitude by using the distance and $L_{\rm all}$.
[c] Observed *K2* magnitude corresponding to $L_{\rm all}$.

on the MK spectral classes (Cox 2000), the derived radius is significantly smaller than that of a normal isolated main sequence star. Furthermore, the mass and radius also conflict with the semi-empirical mass-period and radius-period relations of CV secondary (Smith & Dhillon 1998; Warner 2003) shown in the two right-hand panels of Figure 4.

Instead, we created a model with phase zero at the secondary dip of the light curve. Initially, we fixed the inner accretion disk radius to the radius of the white dwarf. However, a convergent solution could not be found. Instead, an accretion disk model with two hotspots and $R_{\rm in}$ much larger than $R_{\rm wd}$ was found to fit the data reasonable well. $R_{\rm in} > R_{\rm wd}$ can be interpreted as a truncation of the accretion disk far from the WD, consistent with the IP classification of RZ Leo by Szkody et al. (2017) and Dai et al. (2016). This means that the physical structure of RZ Leo may be more complex than the simple disk model calculated by XRBinary because accretion curtains near the magnetic poles of the white dwarf may be involved. This may be the reason that the best-fitting light curve derived by XRBinary cannot perfectly describe the secondary hump of RZ Leo. Based on this disk model, CKp$_2$ calculated by using Equation (1) is around 1.5 mag larger than Kp$_2$. This discrepancy is likely to be caused by the lack of an accretion curtain in the disk model. In the future, a complete IP model including the light from an accretion curtain should help correct this difference. In spite of the deviation in the secondary hump and CKp$_2$, limits to two key parameters of the disk ($R_{\rm in}$ and ξ) can be obtained from the double-humped *K2* phased light curve.

According to the typical disk-field interaction models (e.g., Pringle & Rees 1972; Ghosh & Lamb 1978; White & Stella 1988), the corotation radius of a magnetic white dwarf, $R_{\rm co}$, can be calculated using,

$$R_{\rm co} = f_{\rm co} M_{\rm wd}^{1/3} P_{\rm rot}^{2/3}, \qquad (3)$$

where $f_{\rm co} = (GM_{\odot}/4\pi^2 R_{\odot}^3)^{1/3}$, $R_{\rm co}$ and $M_{\rm wd}$ are in solar units, $P_{\rm rot}$ is the spin period of the magnetic white dwarf in unit of seconds. By using the parameters listed in Table 5 and a spin period of 220 s (Dai et al. 2016; Szkody et al. 2017), $R_{\rm co}$ of RZ Leo can be estimated to be 0.085 $R_{\odot}$, which is 17 times larger than $R_{\rm wd} = 0.005\,R_{\odot}$. Considering that the accretion process in RZ Leo is steady (Dai et al. 2017), $R_{\rm in}$ is required to be almost equal to $R_{\rm co}$. However, $R_{\rm in} = 0.211(2)\,R_{\odot}$ is much larger than $R_{\rm co}$. In a typical IP (Ghosh & Lamb 1978), $R_{\rm co}$ is regarded as the inner radius of an unperturbed disk and the transition region of a truncated disk (i.e., located between $R_{\rm co}$

and $R_{\rm in}$) may be actually invisible in the optical band due to a possible disruption of the accretion flow caused by the magnetosphere of the magnetic white dwarf. Since a hotspot on the disk surface always shows $R_{\rm ssmin} < R_{\rm in}$ during the iterations of NMfit, the parameter of $R_{\rm ssmin}$ is fixed to be equal to $R_{\rm in}$. The high effective temperature of this hotspot indicated by $T_{\rm ratio} = 7.2$ indicates that more than 97% of the luminosity of the disk is from this slim and extended hotspot. Moreover, this hotspot is regarded to be a plausible second impact region of an inward and overflowing stream striking onto the magnetosphere of the magnetic white dwarf. This region was previously reported in several IP systems (e.g., EX Hya in outburst, Hellier et al. 1989; and QZ Vir in quiescence, Shafter & Szkody 1984). Note that all three systems are for an unusually short period (under the gap) IPs. Compared to this hotspot, the other hotspot at the edge of the disk is much smaller and cooler. Both edge and surface hotspots are located at the phases 0.723(1) and 0.47(2), respectively. This disk configuration derived in quiescence is consistent with the disk of EX Hya during outburst, with two hotspots at similar phases (Hellier et al. 1989). This disk configuration may be common for IP systems. A low-luminosity truncated disk with $L_d = 2.3 \times 10^{30}$ erg s^{-1} (i.e., the luminosity contribution of the disk is less than 10% of the whole CV system) may be a straightforward conclusion for an IP system like RZ Leo due to the lack of a hot inner part of the disk. Compared with the other four sources of light in RZ Leo (i.e., the two component stars and two hotspots on the disk), the relative flux contributions from this truncated disk shown in Figure 2 are almost negligible (close to zero).

The best-fitting CV model indicates that RZ Leo has a moderate orbital inclination of $61°.0(\pm 0°.9)$ and contains a massive white dwarf and a low mass red dwarf. The mass ratio, $q_{\rm orb} = 0.080(6)$ is within the error bar of that estimated from its superhump excess (Ishioka et al. 2001). The secondary mass and radius (i.e., $M_{\rm rd} = 0.101(8)\,M_{\odot}$ and $R_{\rm rd} = 0.16\,R_{\odot}$) are not only in accord with an isolated red dwarf later than M5V but also support the semi-empirical mass-period and radius-period relations of CV secondaries (Smith & Dhillon 1998; Warner 2003). The small mass transfer rate, $\dot{M}_{\rm rd} \simeq 3.01(\pm 0.07) \times 10^{-12}\,M_{\odot}$ yr^{-1} calculated by using Equation (2), seems to explain the small and cool hotspot at the edge of the disk that is shown in the disk model. Recently, Dubus et al. (2018) showed the average mass transfer rates of a sample of $\sim$130 CVs with a parallax distance in the *Gaia* DR2 catalog. The estimated mass transfer rate of RZ Leo lies
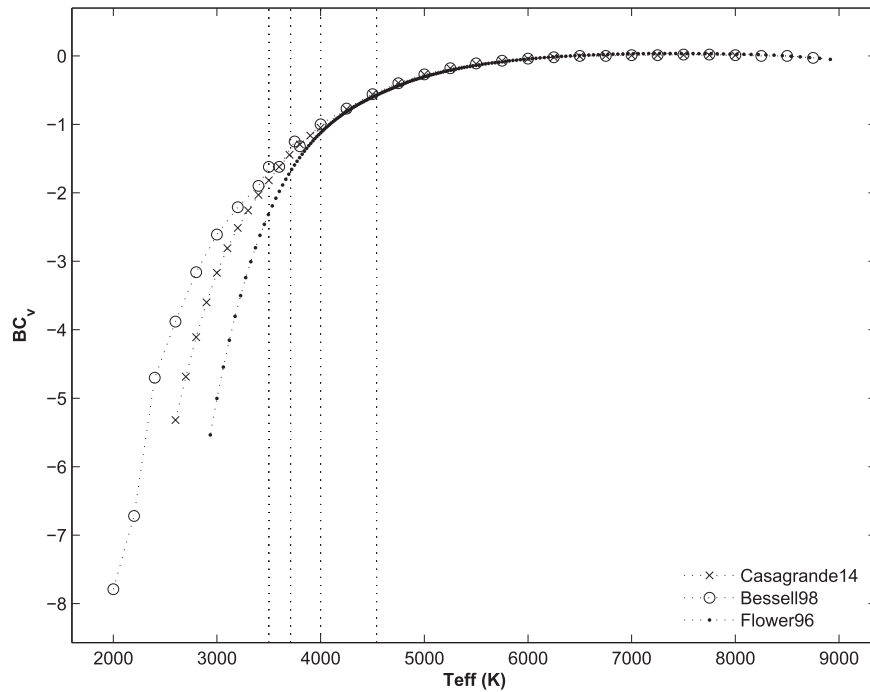
Figure 3. Diagram of bolometric correction in V band (BC$_v$) against the effective temperature of a main sequence star (T_{eff}). Three legends of Casagrande14, Bessell98 and Flower96 refer to the BC$_v$ tabulations given by Casagrande & VandenBerg (2014), Bessell et al. (1998) and Flower (1996), respectively. The four dotted lines from left to right denote T_{rd} of WD 1144+011, RZ Leo, TW Vir and J0632+2536, respectively.

well within the region where a stable, cool disk exists within the system. This explains a lack of DN outbursts for RZ Leo. $\tau_{\dot{M}} \sim 3.4 \times 10^{10}$ year calculated from the mass transfer rate is larger than τ_{kh} of the secondary. The derived secondary mass and radius further confirm that the secondary of RZ Leo is in thermal equilibrium, since they are consistent with the mass–radius relation of the isolated main sequence stars shown in the bottom left-hand panel of Figure 4. Since $T_{rd} = 3710(\pm30)$ K suggests a slightly earlier spectral type than M5V, this higher T_{rd} may be attributed to irradiation of the companion. Due to $L_{rd} > L_{wd} + L_d$, the irradiation effect is not calculated by XRBinary. However, the maximal $F_{irr} \sim 1.54$ that is shown in Figure 5 indicates a significant irradiation effect in RZ Leo. A prominent irradiation effect can be expected in an IP system because the white dwarf primary is not embedded in the truncated thin disk. Furthermore, the small disk of RZ Leo implies that the irradiation region is visible at phase 0.5 despite the similar orbital inclination to that of J0632+2536. Although $F_{obs} \sim 0.93$ does not seem to support a large irradiation effect, the presence of an accretion curtain and a brighter second impact region complicate an accurate calculation of the irradiation effect in RZ Leo.

7.3. TW Vir

By using infrared photometry, the secondary is estimated to be a M3V star with a mass of 0.43 $M_\odot$ and a radius of 0.48 $R_\odot$ (Mateo et al. 1985). According to the MK spectral classes (Cox 2000), the initial temperature of the secondary was set to be 3367 K. Based on the mass ratio of 0.44 (Shafter 1983), the white dwarf mass of TW Vir is calculated to be 0.98 $M_\odot$. Since no accurate white dwarf temperature has been obtained from the UV spectra (Córdova & Mason 1982; Szkody 1985; Hamilton et al. 2007), and TW Vir is a long period (above the gap) system with an orbital period of 0.182682(3) day derived from the K2 data Dai et al. (2017), we set the same initial white dwarf

temperature as that of J0632+2536. Because the secondary hump of TW Vir is not located at orbital phase 0.25 or 0.75, model-2 is used for the calculations. Two phased light curves corresponding to phase zero at the primary and at the secondary dips were used to derive two disk models, respectively. In these two disk models, three parameters involving the positions of two hotspots on the disk in ζ direction (i.e., ζ_{esmid}, ζ_{ssmin} and ζ_{ssmax}) show nearly constant phase differences of 0.5, while all of the remaining parameters are almost the same. Therefore, both models are not significantly different and the double-hump modulation of TW Vir is mainly caused by the two hotspots on the disk.

Since the χ^2 of the model based on the phased light curve with phase zero around the secondary dip is slightly smaller than that with phase zero at the primary dip, the primary hump was set to phase at 0.75 and the corresponding model is analyzed in the following discussion. The two best-fitting orbital parameters: $q_{orb} = 0.41(\pm0.05)$ and $i_{orb} = 44°.3(\pm0°.5)$ listed in Table 5 are consistent with the previous results derived from the infrared and UV data (Córdova & Mason 1982; Mateo et al. 1985). The derived mass ratio confirms the previous classification of TW Vir as a U Gem type DN (O'Connell 1932) but the derived orbital inclination is smaller than that obtained by Hamilton et al. (2007). The calculated CKp$_2$ listed in Table 4 suggests that the best-fitting model of TW Vir is consistent with the *Gaia* distance. The relative flux contributions from the hotspot at the edge of the disk around phase 0.75 shown in Figure 2 almost perfectly reproduces the significant primary hump, which lasts for over half of an orbit. Although the other hotspot appearing on the outer radius of the disk covers a long phase width of 0.42, the small $T_{ratio}^{ss} = 1.20$ (±0.02) may explain its small relative flux contributions, as shown in Figure 2. Like RZ Leo, the relative flux contribution from the disk is close to zero. The derived mass and radius of the secondary fits with the semi-empirical secondary mass-period and radius-period relations (Smith & Dhillon 1998;

Table 5
Photometric Solutions for Three DN

Parameter[a]	J0632+2536	RZ Leo	TW Vir
Model type[b]	Model-1	Model-2	Model-2[irr]
Orbit			
$q_{orb}(M_{rd}/M_{wd})$	0.8(1)	0.080(6)	0.41(5)
i_{orb} (degree)	60.3(5)	61.0(9)	44.3(5)
White dwarf			
$M_{wd}(M_\odot)$	0.81(8)	1.26(3)	1.10(3)
$R_{wd}(R_\odot)^c$	0.01	0.005	0.007
$T_{wd}^{\ d}$	25.4	15.0	19.1
$L_{wd}^{\ c}$	1.5	0.045	0.23
Red dwarf			
$M_{rd}(M_\odot)$	0.7(1)	0.101(8)	0.45(6)
$R_{rd}(R_\odot)^c$	0.81	0.16	0.48
T_{rd}	4.54(8)	3.71(3)	4.00(4)
$L_{rd}^{\ c}$	9.6	0.17	2.0
Accretion disk			
$R_{in}(R_\odot)$	0.01[d]	0.211(2)	0.007[d]
$R_{out}(R_\odot)$	1.22(1)	0.401(2)	0.536(3)
$H_{edge}(R_\odot)$	0.091(4)	0.0801(6)	0.1174(3)
ξ	−0.11[e]	−0.12(6)	−0.11(4)
L_{d0}	3.9(3)	0.00061(6)	3.36(6)
$L_d^{\ c}$	4.1	0.023	4.0
Hotspot at the edge of the disk			
T_{es}	6.2(1)	3.71(2)	4.80(2)
ζ_{esmid} (phase)	0.844(2)	0.723(1)	0.727(6)
$\zeta_{eswidth}$ (phase)	0.033(2)	0.057(4)	0.296(3)
Hotspot on the surface of disk			
ζ_{ssmin} (phase)	⋯	0.38(2)	0.32(5)
ζ_{ssmax} (phase)	⋯	0.56(2)	0.74(3)
$R_{ssmin}(R_\odot)$	⋯	0.211[e]	0.489(8)
$R_{ssmax}(R_\odot)$	⋯	0.217(5)	0.536[e]
T_{ratio}^{ss}	⋯	7.2(2)	1.20(2)
χ^2	11.9	2.3	0.66

Notes.
[a] The unit of temperature and luminosity is 10^3 K and 10^{32} erg s^{-1}, respectively.
[b] The model with a superscript "irr" denotes that the irradiation effect is included in XRBinary.
[c] Calculated by XRBinary.
[d] Fixed in NMfit program.
[e] Insensitive to the observed light curves.

Warner 2003). This indicates that the spectral type of the secondary is close to M2V, which is similar to the result from infrared photometry (Mateo et al. 1985). However, compared with the K5V star of J0632+2536 and the M5V star of RZ Leo, the M2V star of TW Vir never shows large-amplitude ellipsoidal modulations. Instead, it gives rise to a small amplitude second hump in the phased light curve. By using Equation (2), the estimated $\dot{M}_{rd}$ listed in Table 6 indicates that $\tau_{\dot{M}} \sim 9 \, \tau_{kh}$, which is common for most CV secondaries (Patterson 1984). A somewhat oversized secondary of TW Vir relative to an isolated main sequence star of the same mass is not obtained, implying that $\dot{M}_{rd}$ may be overestimated.

Like J0632+2536, $T_{eff} = 4850$ K listed in Table 4 is higher than the derived $T_{rd} = 4000(\pm40)$ K. This may imply that the

higher T_{eff} derived by *Gaia* is common for DN due to the possible contributions from hotter components in these systems (e.g., the white dwarf and accretion disk). Since T_{rd} is obviously higher than the effective temperature of the M2V star shown in Figure 4, we investigated the irradiation effect of the secondary in this system. Note that TW Vir is the only object with $L_{rd} < L_{wd} + L_d$. Accordingly, the calculation of irradiation was included in XRBinary. However, both light curves calculated with and without irradiation by XRBinary are almost identical. Hence, irradiation in TW Vir may be weak, which is also demonstrated by $F_{obs} \sim 1$ with two minima in the light curve at almost the same flux level. Since L_d calculated from a near-flat temperature distribution with a power index of −0.11(±0.04) is nearly two times L_{rd}, and the total contributions of two hotspots
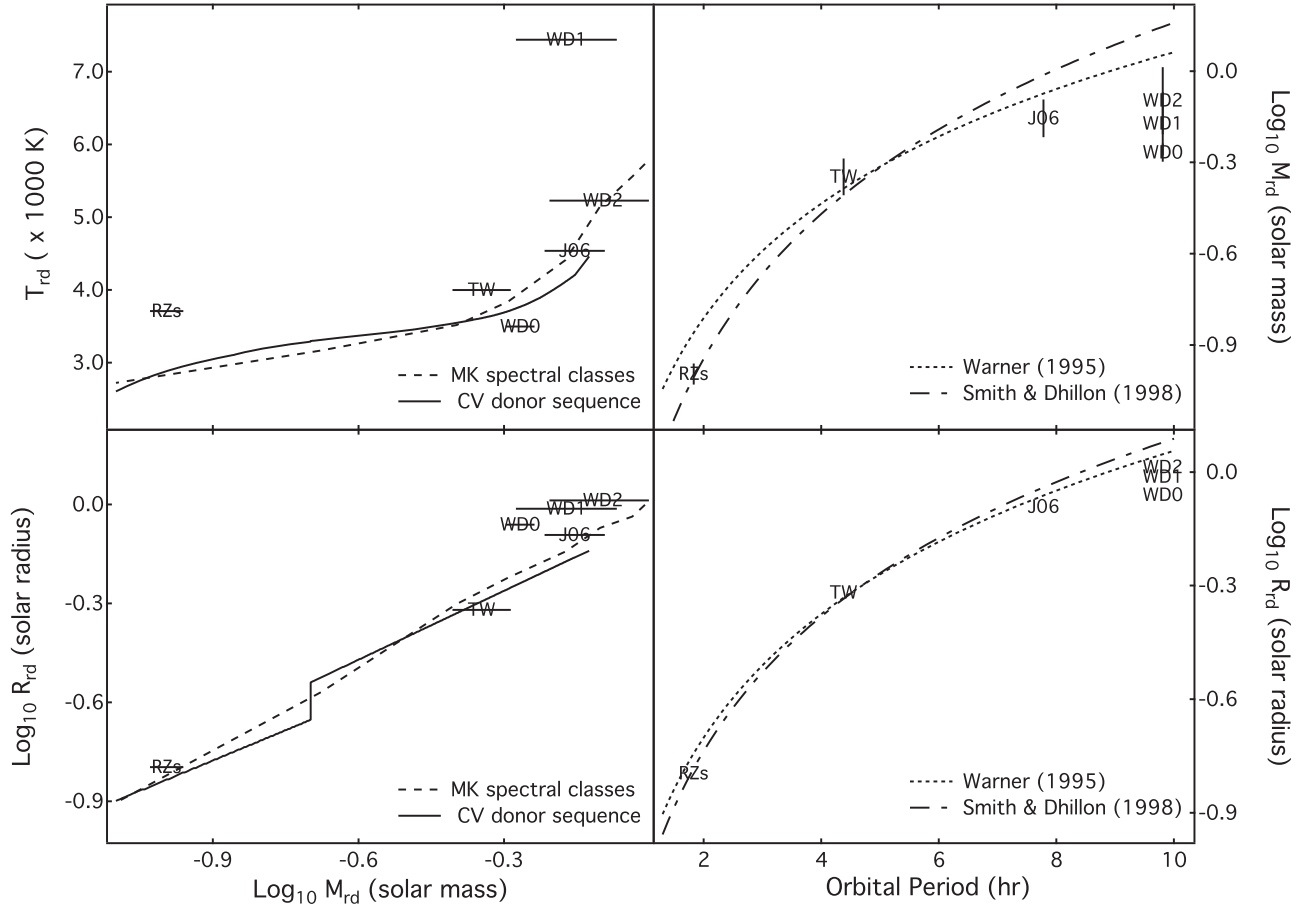
Figure 4. Four relationships of the secondaries. Top left-hand panel: the relationship of the logarithm of mass and the effective temperature. Bottom left-hand panel: the logarithm of mass–radius relationship. Top right-hand panel: the period–mass relationship. Bottom right-hand panel: the period–radius relationship. The dashed and solid lines denote the relationships based on the isolated low-mass stars (Cox 2000), and the semi-empirical CV donor sequence (Knigge 2006; Knigge et al. 2011), respectively. The dashed–dotted and dotted lines describe the relationships derived by Smith & Dhillon (1998) and Warner (2003), respectively. The symbols of the data points are the same as those used in Figure 1.

Table 6
The Estimated Parameters of the Secondaries of Four Systems

Name[a]	$\dot{M}_{rd}$	$\tau_{\dot{M}}$	τ_{kh}	$\tau_{\dot{M}}/\tau_{kh}$
	$10^{-10}\ M_\odot\ yr^{-1}$	10^9 year	10^9 year	
J0632+2536	2.5(±0.2)	2.8(±0.5)	0.076	37
RZ Leo	0.0311 (±0.0008)	32.4(±2.7)	0.45	72
TW Vir	1.92(±0.05)	2.3(±0.3)	0.25	9
WD 1144 +011[b]	67.8(±16.0)	0.1(±0.03)	0.006	18
WD 1144 +011[c]	7.9(±1.8)	1.0(±0.3)	0.027	37

Notes.
[a] Calculations by using the parameters listed in Tables 5 and 7.
[b] For the model-1.
[c] For the model-2.

are only 16% of L_d, the weak irradiation effect of the secondary is overpowered in the light curve. Large variations in the disk luminosity may further weaken the ability to detect irradiation. There are, however, two issues which further complicate our conclusions. The first is that the orbital modulation of TW Vir shown in Figure 2 is only extracted from the part of the quiescent light curve around its superoutburst. The second is that the

double-hump modulation does not always maintain stability, and the secondary hump has a small amplitude and shows a large scatter in the unbinned light curve (Dai et al. 2017). Further analysis of its light curves at different times may reveal more details of the irradiation effect in TW Vir.

7.4. WD 1144+011

This poorly understood variable star is classified as a DA+dMe binary from a single optical spectrum obtained by Berg et al. (1992). For comparison with this spectrum obtained over 20 years ago, a new spectrum was taken on 2017 January 22 by using the BFOSC spectrograph attached to the Xinglong Observatory 2.16 m telescope (XL 216, Fan et al. 2016). This is a better optical spectrum that shows some changes from the original. The details concerning our spectrum are presented in Appendix B. A synthetic analysis based on the single-hump light curve extracted by Dai et al. (2016) can test the possibility of the existence of a disk around the primary white dwarf of WD 1144+011. Considering that WD 1144+011 is a long orbital period system with an orbital period of 9.81 hr (Dai et al. 2016), the initial parameters of the white dwarf are set to be the same as those of J0632+2536. Combined with the parameters of a M dwarf, all three models were used to attempt to reproduce the stable single-hump modulation that is apparent in the K2 light curve.
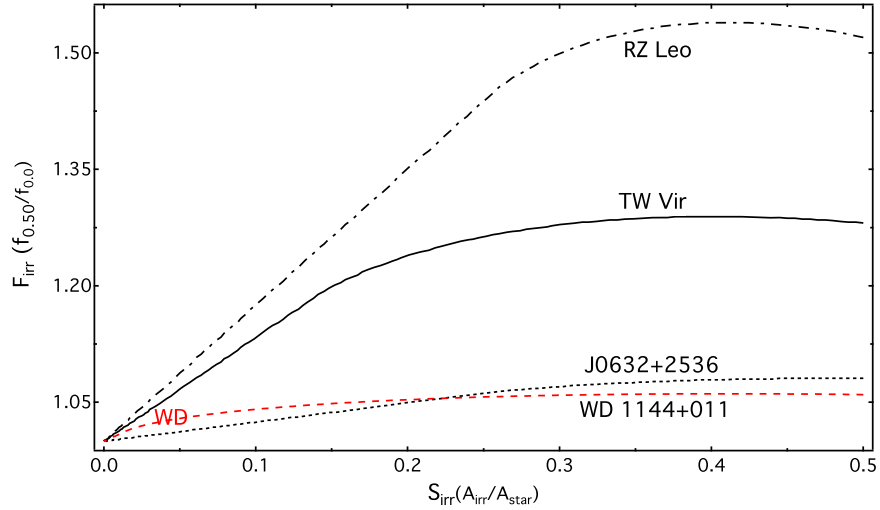
Figure 5. Diagram of the flux ratio between phases 0.5 and 0.0, F_{irr}, changing along with a normalized area of the irradiation region S_{irr}. The red symbol WD denotes $S_{\mathrm{irr}} \sim 0.05$ corresponding to $F_{\mathrm{obs}} = 1.03$ estimated from the single-hump modulation of WD 1144+011.

7.4.1. Model Without a Disk

In principle, model-0 can only produce ellipsoidal modulation caused by the orbital motion of the Roche-lobe filling secondary. The asymmetry shown in the single-hump modulation of WD 1144+011 cannot be explained by a pure ellipsoidal modulation derived from model-0. Moreover, the irradiation effect in WD 1144+011 that was calculated by XRBinary cannot resolve this problem because its long orbital period may imply a bright secondary like J0632+2536 (i.e., $L_{\mathrm{rd}} > L_{\mathrm{wd}}$). In spite of this, an irradiation region on the surface of the secondary was added to allow for an asymmetrical single-hump modulation (i.e., a bump on the rise to the maximum). We assumed that this irradiation region is a circular bright starspot on the secondary, which can be easily calculated by XRBinary. Since the single-hump modulation of WD 1144+011 observed in K2-C1 is very stable (lasting at least a complete campaign periods of ~ 3 months, Dai et al. 2016), a stable region due to irradiation of the secondary may be more plausible to explain this long-term steady modulation than a variable starspot on an active M type dwarf.

In XRBinary, a starspot on the secondary can be described by the four parameters (i.e., θ^{sp}, ϕ^{sp}, R^{sp} and $T^{\mathrm{sp}}_{\mathrm{ratio}}$)[17]. For WD 1144+011, this *starspot* is assumed to be a hotspot (i.e., $T^{\mathrm{sp}}_{\mathrm{ratio}} > 1$). All of the parameters including four component parameters (M_{wd}, T_{wd}, q_{orb} and T_{rd}) and four parameters of the starspot were set to be adjustable in NMfit. The derived $M_{\mathrm{wd}} = 1.11(8) M_{\odot}$ is almost the same as that of TW Vir shown in Figure 1, while $T_{\mathrm{wd}} = 27{,}100\,K$ suggests a hotter and brighter white dwarf. Compared with the three DN, WD 1144+011 is the only object with a slightly cooler M dwarf ($T_{\mathrm{rd}} = 3500(\pm100)\,K$) than the predicted mass–temperature relation of the semi-empirical CV donor sequence (Knigge 2006; Knigge et al. 2011). This is consistent with $T_{\mathrm{eff}} = 3657.5\,K$ shown in the *Gaia* database. Compared with the higher T_{eff} of the two DN J0632+2536 and TW Vir, this compatible T_{eff} can be explained by the lack of a disk around the white dwarf. Since the companion star in

WD 1144+011 is cooler than the secondaries in the other systems discussed here, it has the largest uncertainty in BC_v, as shown in Figure 3. This is reflected in the large range of derived CKp_2 (14.8 $\sim$ 16.2 mag), which is consistent with the corresponding Kp_2 value listed in Table 4. Like TW Vir, the ellipsoidal modulations caused by the M star never dominates the orbital modulation. The mass and radius of the secondary deviate from all the mass–radius, mass-period and radius-period relations shown in Figure 4. Note that both semi-empirical mass-period and radius-period relations are only available in the period range of 1.3 $\sim$ 9 hr (Smith & Dhillon 1998; Warner 2003). With an orbital period of 9.81 hr, WD 1144+011 is beyond this period range. The bottom left-hand panel of Figure 4 shows that the inflation of the secondary is about 38%. Besides the known inefficient mechanisms of donor bloating (e.g., tidal deformation, rotational deformation and irradiation of the secondary) discussed by Knigge et al. (2011), the deviation from thermal equilibrium of the secondary caused by the donor mass loss can result in a large donor inflation of up to 20% $\sim$ 30% (Patterson 2005; Knigge 2006). However, this mass loss mechanism is still not enough to explain the derived inflated secondary star.

Although both light curves calculated with and without irradiation by XRBinary are almost identical due to $L_{\mathrm{rd}} > L_{\mathrm{wd}}$, the final χ^2 of model-0^{irr} is slightly smaller than that of model-0. Thus, the best-fitting parameters and their uncertainties listed in Table 7 are calculated using model-0^{irr}. The reproduced light curves and the corresponding 2D pre-CV configuration are shown in the top left-hand and right-hand panels of Figure 6, respectively. This detached binary configuration with a low inclination of $14°\!.3(\pm0°\!.4)$ supports the previous classification of WD 1144+011 as a pre-CV system (i.e., a DA+dMe detached system). Our model also shows that the orbital variation seen in the light curve is dominated by the hotspot on the secondary's surface. Compared with the three DN, the pre-CV WD 1144+011 is the only object with $F_{\mathrm{obs}} = 1.03$ larger than 1. Thus, $T^{\mathrm{sp}}_{\mathrm{ratio}} = 1.097(\pm0.003)$ combined with F_{obs} suggests that the calculated irradiation region may be a good representation of the physical picture of WD 1144+011. The effective temperature of the starspot can be estimated to be around 3900 K based on $T^{\mathrm{sp}}_{\mathrm{ratio}}$. A relation between F_{irr} and S_{irr} shown in Figure 5 indicates weak irradiation in WD 1144+011, similar to J0632+2536, and $S_{\mathrm{irr}} \sim 0.5$ corresponding to

---

[17] θ^{sp} and ϕ^{sp} are the coordinates of the spot center in the spherical polar coordinate system. $\phi^{\mathrm{sp}} = 0$ direction lies in the orbital plane and points in the direction of motion of the secondary in its orbit. ϕ^{sp} increases in a right-handed sense about the $\theta^{\mathrm{sp}} = 0$ direction. R^{sp} is the angular radius of the spot as seen from the center of the secondary star. $T^{\mathrm{sp}}_{\mathrm{ratio}}$ is the ratio of the starspot temperature to the local effective temperature of the unspotted star.
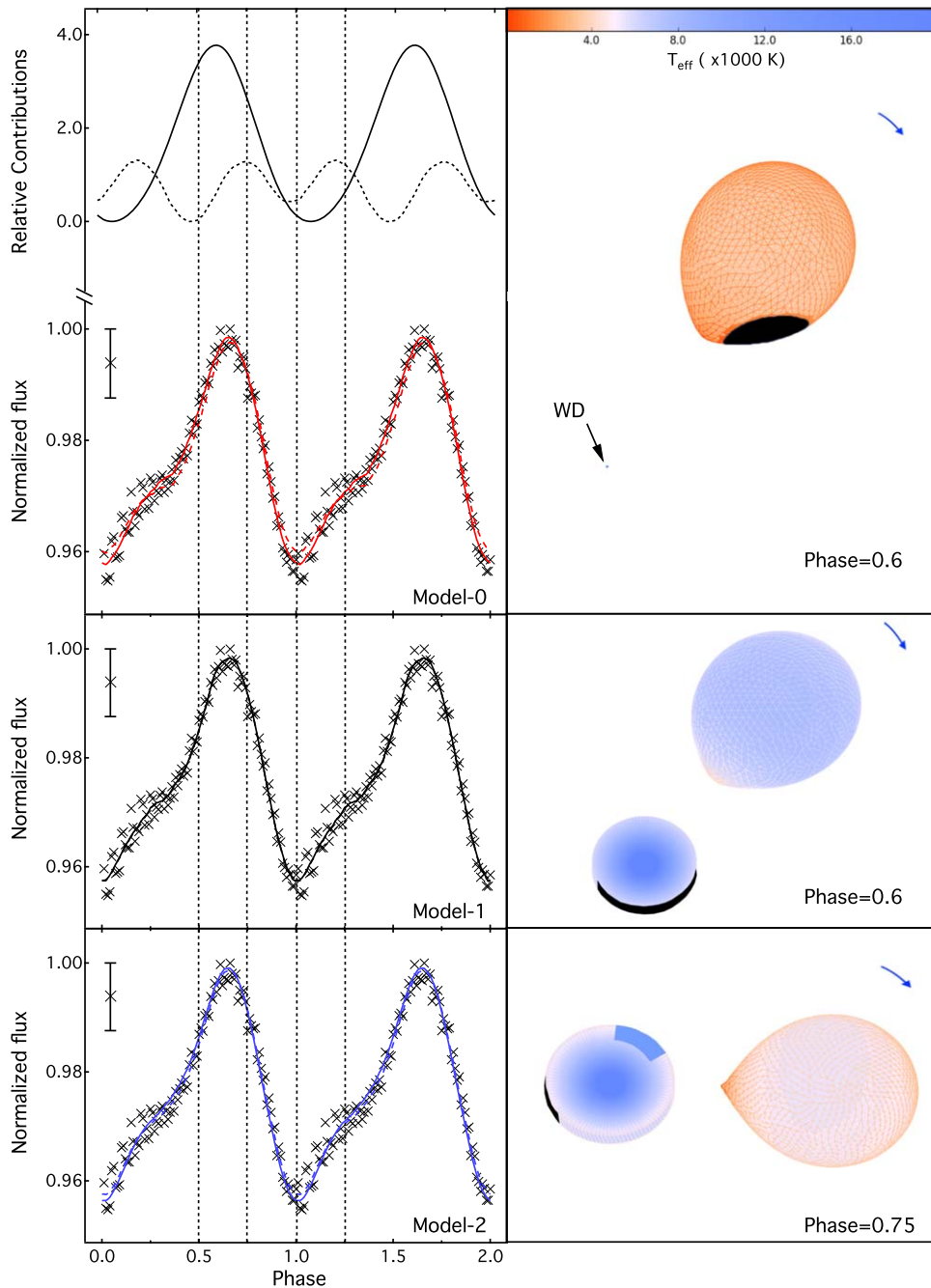
Figure 6. The phased and binned light curve of WD 1144+011 superimposed with the best-fitting light curves denoting with the red, black and blue lines calculated by using the model-0, model-1 and model-2 are plotted in the top, middle and bottom left-hand panels, respectively. The solid and dash lines respectively refer to two types of calculations including and excluding the irradiation effect in XRBinary. The three right-hand panels from the top to bottom show the corresponding 2D binary configurations at phases 0.6, 0.6 and 0.75, respectively. All symbols are the same as that of Figure 2.

$F_{obs} = 1.03$ is consistent with the size of the starspot calculated from $R^{sp} = 27\overset{\circ}{.}7(\pm0\overset{\circ}{.}7)$. Due to the lack of an accretion disk, this irradiation region is much smaller than the typical size of an irradiation region in a CV (Davey & Smith 1992).

7.4.2. Model With a Disk

Since an extra light source is imperative to explain the asymmetrical single-hump modulation, model-1 and model-2 were investigated. All of the adjustable parameters and their uncertainties are listed in Table 7. $\dot{M}_{rd}$ is estimated for both models and is given in Table 6. The white dwarf mass of model-1 is smaller than the prediction of the average white dwarf mass in a CV with the

same orbital period (Ritter & Burkert 1986; Zorotovic et al. 2011). T_{wd} from both of the disk models is consistent with T_{wd} from the non-disk model, suggesting that WD 1144+011 does contain a hot white dwarf. The final χ^2 of the two disk models are almost the same as that of the non-disk model-0. All three models imply an oversized secondary with generally consistent masses and radii. The top left-hand panel of Figure 4 shows that the secondary of model-1 has an extremely high effective temperature, which is over twice the average effective temperature of an M dwarf. Although the secondary of model-2 agrees with a G9V star based on the MK spectral classes (Cox 2000), a spectral type of G9V contradicts with our spectrum. Compared with the *Gaia* distance

Table 7
Three Photometric Solutions for the Pre-CV WD 1144+011

Parameters[a]	WD 1144+011		
Model type[b]	Model-0[irr]	Model-1	Model-2
Orbit			
$q_{orb}(M_{rd}/M_{wd})$	0.49(2)	0.99(2)	0.92(9)
i_{orb} (degree)	14.3(4)	17.7(4)	26.3(6)
White dwarf			
$M_{wd}(M_{\odot})$	1.11(8)	0.68(16)	0.9(2)
$R_{wd}(R_{\odot})$[c]	0.007	0.012	0.009
T_{wd}^{d}	27.1	27.0	25.7
L_{wd}^{c}	0.91	2.5	1.3
Red dwarf			
$M_{rd}(M_{\odot})$	0.54(4)	0.67(16)	0.8(2)
$R_{rd}(R_{\odot})$[c]	0.87	0.97	1.03
T_{rd}	3.5(1)	7.44(7)	5.23(6)
L_{rd}^{c}	4.1	100.7	27.7
Bright starspot on the red dwarf			
θ^{sp} (degree)	38(3)	…	…
ϕ^{sp} (degree)	0.2[e]	…	…
R^{sp} (degree)	27.7(7)	…	…
T_{ratio}^{sp}	1.097(3)	…	…
Accretion disk			
$R_{in}(R_{\odot})$	…	0.01[d]	0.009[d]
$R_{out}(R_{\odot})$	…	0.597(5)	0.808(8)
$H_{edge}(R_{\odot})$	…	0.363(8)	0.176(3)
ξ	…	−0.11[e]	−0.18(4)
L_{d0}	…	13.7(±2.7)	13.5(±2.3)
L_{d}^{c}	…	23.0	19.4
Hotspot at the edge of the disk			
T_{es}	…	6.50(5)	5.38(7)
ζ_{esmid} (phase)	…	0.623(4)	0.548(8)
$\zeta_{eswidth}$ (phase)	…	0.41(2)	0.17(1)
Hotspot on the surface of disk			
ζ_{ssmin} (phase)	…	…	0.129(6)
ζ_{ssmax} (phase)	…	…	0.221(2)
$R_{ssmin}(R_{\odot})$	…	…	0.605(1)
$R_{ssmax}(R_{\odot})$	…	…	0.808[e]
T_{ratio}^{ss}	…	…	1.90(4)
χ^2	8.6	7.9	8.8

Note. All footnotes are the same as those of Table 5.

of WD 1144+011 listed in Table 4, both L_{rd} for the model-1 and model-2 are too large. Hence, the consistency of the effective temperature may be only coincidental. To recheck the deviations in T_{rd} in model-1 and model-2, T_{rd} was fixed to be 3500 K in line with the secondary temperature found using model-0. However, no convergent solution could be obtained. In spite of $L_{rd} > L_{wd} + L_{d}$, irradiation was still included in these models. Like model-0, the light curves calculated with and without irradiation for the two disk models only show small discrepancies around phases 0.5 and 0.0. Both calculated F_{irr} are far larger than F_{obs}. This means that the assumed large irradiation of the secondary is not supported by the K2 data. Compared with the pre-CV configuration obtained from model-0, the two models with

an accretion disk are not convincing. As such, our modeling based on the K2 phased light curve provides further evidence for the classification of WD 1144+011 as a detached pre-CV system.

8. Conclusions

8.1. Synthetic Codes

Based on the light curve synthesis code XRBinary derived by E. L. Robinson, NMfit was developed to analyze the light curves of the four low-inclination systems: J0632+2536, RZ Leo, TW Vir and WD 1144+011. All of the parameters of the best-fitting models and their uncertainties are estimated by NMfit. Additionally, Phoebe 2.0 was used to visualize the configuration of each system using each systems' best-fitting parameters. Since phase zero is hard to identify in any low-inclination CV system with a double-hump modulation due to the lack of a significant eclipse feature, we tested models that had phase zero located at either the primary or secondary minimum, and we chose the model which matched the observed light curve best. Except for WD 1144+011, which had a single maximum in its phased orbital light curve, the derived CV models of the other three DN indicate that phase zero should be placed at the secondary minimum.

8.2. Physical Models

For J0632+2536 and TW Vir, the best-fit disk models show that the primary hump is mostly due to the hotspot at the edge of the disk, which is a key indicator of mass transfer via the L1 point. Another hotspot on the disk surface can explain the phase difference between the two humps of the double-hump modulations. For WD 1144+011, the bright starspot representing irradiation of the secondary star is responsible for the modulation seen in the optical light curve.

The lack of an accretion curtain in the disk model of RZ Leo implies that this model may not be appropriate for a comparison with the measured distance by *Gaia*. The derived physical models of the other three binary systems are consistent with the results from *Gaia* DR2. The flat power law index of the disk found in all three DN models ($\xi \sim -0.11$) is similar to previous observations (e.g., Wood & Crawford 1986; Wood et al. 1989; Rutkowski et al. 2016) and supports the theory that a quiescent CV disk deviates from the temperature distribution of a typical steady-state disk. A low-luminosity accretion disk model of RZ Leo derived from its K2 light curve further confirms that RZ Leo is an IP system with two hotspots on a truncated disk. One of the hotspots on the disk surface contributes a significant fraction of the disk luminosity (>97% of L_{d}), and is located at the inner edge rather than the outer edge of the disk. This may be evidence of an impact region between an inward and overflowing stream and the magnetosphere of the magnetic white dwarf. Compared with RZ Leo, the small hotspot of J0632+2536 and two hotspots of TW Vir covering large phase ranges are only small contributors to the disk luminosity. Our spectrum of WD 1144+011 with a relatively flat continuum and H_{α} emission supports its previous classification as a DA+dMe system (Berg et al. 1992). We note that WD 1144+011 shows different flux levels in the continuum and emission lines. The model light curve based on the asymmetrical single-hump modulation requires an extra light source (i.e., a weak irradiation region of the secondary rather than a large hotspot at the edge of the disk) to explain the modulation of WD 1144+011.

8.3. The Secondaries

The estimated $\dot{M}_{rd}$ for all four objects are within a range of $10^{-9} \sim 10^{-12} \, M_\odot \, yr^{-1}$. Except for the pre-CV WD 1144 +011, which contains an oversized secondary, the other three DN have secondaries in thermal equilibrium with masses and radii conforming to the semi-empirical CV donor sequence (Knigge 2006; Knigge et al. 2011) and MK spectral classes (Cox 2000). The derived effective temperatures of all three DN are significantly higher than predicted. Hence, a DN system containing a substantially hotter secondary may be a common feature rather than a peculiarity. This can be attributed to irradiation of the secondary because T_{rd} calculated from L_{rd} is an average parameter that can be increased by irradiation. Compared with T_{eff} listed in the *Gaia* catalog, the lower T_{rd} of the two DN J0632+2536 and TW Vir may be due to contamination from a hot white dwarf and disk. This is further supported by the T_{rd} of the pre-CV WD1144+011, which is almost consistent with the *Gaia* T_{eff}. It should also be noted that the *Gaia* temperatures are determined from three broad bandpasses (Andrae et al. 2018) and the DR2 release notes urge caution in using them.[18]

Although the double-hump modulation of J0632+2536 can be explained by the partial occultation of the irradiation region on the surface of the secondary due to a large disk and a moderate orbital inclination, investigation of irradiation in the other two DN implies that the effect of irradiation in a CV system is complicated and blended with other modulations. The flux contribution from the secondary of TW Vir is the lowest (i.e., $L_{rd} < L_{wd} + L_d$) among all four objects. Weak irradiation may exist in the DN TW Vir and the pre-CV WD 1144+011. The former can be further tested by additional light curves obtained when the double-hump variation is evident, while the latter can be further checked by taking a time series of spectra over the course of the complete orbital period of 9.81 hr.

Appendix A
A Simple Calculation for the Irradiation Effect of the Secondary in a Low-inclination CV System

Assuming that the secondary is a sphere and the irradiation region with a higher effective temperature of T_{irr} is axisymmetric with the line between the center points of the two component stars, the area of the complete irradiation region S_{irr} can be calculated by the following formula,

$$A_{irr} = 2\pi R_{rd}^2 (1 - \cos\theta), \tag{4}$$

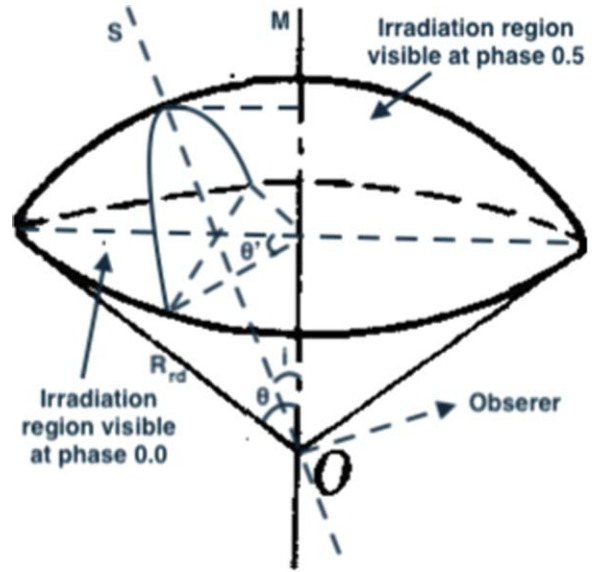[18] https://gea.esac.esa.int/archive/documentation/GDR2/

Figure 7. This sketch displays an irradiation region of the secondary star with a segment shape. The center of the secondary is at O point. The OM line is located on the orbital plane, while the OS line indicates a plane vertical to the line of sight. θ is the half of the opening angle of the irradiation region.

where R_{rd} and θ are the radius of the secondary and the half opening angle of the irradiation region shown in Figure 7, respectively. Therefore, θ should be in a range of $0 \sim \pi/2$. Due to the projection effect (i.e., the orbital inclination less than 90°), the orbital modulation of the secondary will cause the fraction of the irradiation region seen by an observer to vary over the orbital period. The total flux at an orbital phase ϕ can be described as

$$f_\phi = A'_{irr}(\phi)\sigma \, T_{irr}^4 + [2\pi R_{rd}^2 - A'_{irr}(\phi)] \, \sigma \, T_{star}^4, \tag{5}$$

where $A'_{irr}(\phi)$ and T_{star} are the visible area of the irradiation region at the phase ϕ and the effective temperature of the unirradiated part of the secondary, respectively. Note that Equation (5) never considers the occultation of irradiation region by the white dwarf or the disk. In principle, $A'_{irr}(0.0)$ is the minimum, while $A'_{irr}(0.5)$ is the maximum. An inspection of Figure 7 indicates that the former can be estimated by the formula,

$$A'_{irr}(0.0) = \begin{cases} 2R_{rd}^2 \int_i^\theta \theta' \cdot \sin\psi \, d\psi & \theta \geqslant i \\ 0 & \theta < i \end{cases} \tag{6}$$

where i and ψ are the orbital inclination and the second coordinate of the spherical coordinate system, respectively. Moreover, θ' satisfies the following relation,

$$\frac{R_{rd} \sin\psi \cos\theta'}{R_{rd} \sin i} = \frac{R_{rd} \cos\psi}{R_{rd} \cos i}, \tag{7}$$

By combining Equations (6) and (7), $A'_{irr}(0.0)$ can be expressed as,

$$A'_{irr}(0.0) = \begin{cases} 2R_{rd}^2 C_{irr} & \theta \geqslant i \\ 0 & \theta < i \end{cases} \tag{8}$$
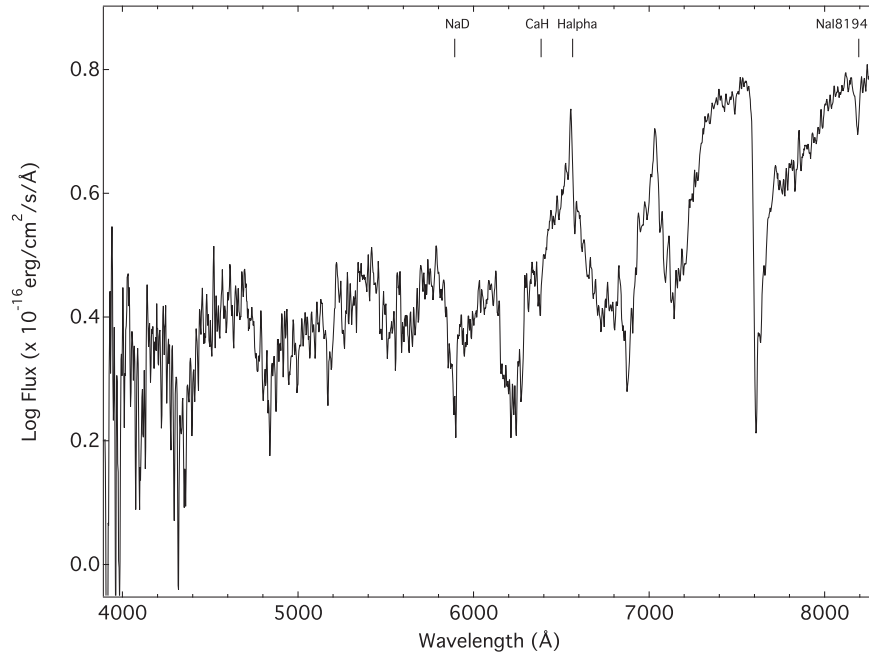
Figure 8. The optical spectrum of WD 1144+011 covering a wavelength range from 3900 Å to 8300 Å was taken by using the Xinglong 2.16 m telescope on 2017 January 22. The characteristic spectral lines are marked.

where $C_{\mathrm{irr}} = \int_i^\theta \arccos(\frac{\tan i}{\tan \psi}) \cdot \sin \psi \, d\psi$. Based on $A'_{\mathrm{irr}}(0.0)$, $A'_{\mathrm{irr}}(0.5)$ can be expressed as,

$$A'_{\mathrm{irr}}(0.5) = \begin{cases} A_{\mathrm{irr}} - A'_{\mathrm{irr}}(0.0) & \theta \geqslant i \\ A_{\mathrm{irr}} & \theta < i \end{cases} \quad (9)$$

By using Equation (5), the flux ratio between the phases 0.5 and 0.0 (i.e., $F_{\mathrm{irr}} = f_{0.5}/f_{0.0}$) can be calculated for a given θ. Based on the normalized area of the irradiation region, $S_{\mathrm{irr}} = A_{\mathrm{irr}}/A_{\mathrm{star}}$ (i.e., $\cos \theta = 1 - 2 S_{\mathrm{irr}}$), F_{irr} can be described as,

$$\begin{aligned} &F_{\mathrm{irr}} \\ &= \begin{cases} \dfrac{(\pi - 2\pi S_{\mathrm{irr}} - C_{\mathrm{irr}}) T_{\mathrm{star}}^4 + (2\pi S_{\mathrm{irr}} - C_{\mathrm{irr}}) T_{\mathrm{irr}}^4}{(\pi - C_{\mathrm{irr}}) T_{\mathrm{star}}^4 + C_{\mathrm{irr}} T_{\mathrm{irr}}^4} & \theta \geqslant i \\ (1 - 2 S_{\mathrm{irr}})\left[\dfrac{T_{\mathrm{irr}}}{T_{\mathrm{star}}}\right]^4 - 2(1 + S_{\mathrm{irr}}) & \theta < i \end{cases} \end{aligned}$$
$$(10)$$

The relations of F_{irr} versus S_{irr} for the three DN and one pre-CV system discussed here are plotted in Figure 5.

Appendix B
A New Observed Optical Spectrum of WD 1144+011

A 1.8 arcsec slit and the G4 grating with a low resolution of 1953 (i.e., 2.97 Å pixel^{-1}) was used with an exposure time of 1800 s. Flux standards and FeAr lamps were used along with IRAF[19] reductions to produce the final calibrated spectrum shown in Figure 8.

This spectrum is dominated by a strong and fairly broad H$_\alpha$ emission line and several molecular absorption bands (e.g., MgH 5211 Å and CaH 6358 Å), and is similar to the previous spectrum obtained by Berg et al. (1992). Thus, our spectrum supports the previous spectral classification of WD 1144+011 derived by (Berg et al. 1992). An active M star can show variable H$_\alpha$ in emission. However, our spectrum shows a flatter blue continuum with a higher red flux level. The measured average equivalent width of H$_\alpha$ is close to 100 Å, although this line is difficult to measure accurately due to the uncertainty of the continuum. It is clear from both our spectrum and that of Berg et al. (1992) that there is no prominent blue continuum from a hot white dwarf or disk and that the Balmer lines are in emission and of variable strength. The changes in flux levels between our spectrum and the spectrum presented in Berg et al. (1992) could be due to phase differences when the two spectra were taken.

ORCID iDs

Zhibin Dai (戴智斌) ⓘ https://orcid.org/0000-0002-4280-6630
Paula Szkody ⓘ https://orcid.org/0000-0003-4373-7777
Mark Kennedy ⓘ https://orcid.org/0000-0001-6894-6044
Jie Su (苏杰) ⓘ https://orcid.org/0000-0001-7566-9436
Peter M. Garnavich ⓘ https://orcid.org/0000-0003-4069-2817

References

Andrae, R., Fouesneau, M., Creevey, O., et al. 2018, A&A, 616, A8
Bailey, J., & Cropper, M. 1991, MNRAS, 253, 27
Bailey, J., Wickramasinghe, D. T., Hough, J. H., & Cropper, M. 1988, MNRAS, 234, 19
Bąkowska, K., & Olech, A. 2015, AcA, 65, 351
Berg, C., Wegner, G., & Foltz, C. B. 1992, ApJS, 78, 409
Bessell, M. S., Castelli, F., & Plez, B. 1998, A&A, 333, 231
Bruch, A. 1996, A&A, 312, 97
Casagrande, L., & VandenBerg, D. A. 2014, MNRAS, 444, 392
Cook, M. C., & Waner, B. 1984, MNRAS, 207, 705
Córdova, H., & Mason, K. O. 1982, ApJ, 260, 716
Cox, A. N. 2000, Allen's Astrophysical Quantities (Springer-Verlag: AIP Press)
Dai, Z. B., & Qian, S. B. 2010a, PASJ, 62, 965

---

[19] IRAF is distributed by the National Optical Astronomy Observatory, which is operated by the Association of Universities for Research in Astronomy (AURA) under cooperative agreement with the National Science Foundation.

Dai, Z. B., Qian, S. B., Fernández Lajús, E., & Baume, G. L. 2010b, MNRAS, 409, 1195
Dai, Z. B., Qian, S. B., & Li, L. J. 2013, ApJ, 774, 153
Dai, Z. B., Szkody, P., Garnavich, P. M., & Kennedy, M. R. 2016, AJ, 152, 5
Dai, Z. B., Szkody, P., Taani, A., Garnavich, P. M., & Kennedy, M. 2017, A&A, 606, 45
Davey, S., & Smith, R. C. 1992, MNRAS, 257, 476
Dubus, G., Otulakowska-Hypka, M., & Lasota, J.-P. 2018, arXiv:1805.02110
Fan, Z., Wang, H., Jiang, X., et al. 2016, PASP, 128, 115005
Fang, K. T. 1980, Acta Mathematice Applicatae Sinica, 3, 363
Feline, W. J., Dhillon, V. S., Marsh, T. R., & Brinkworth, C. S. 2004, MNRAS, 355, 1
Flower, P. J. 1996, ApJ, 469, 355
Frank, J., King, A., & Raine, D. 1992, Accretion Power in Astrophysics (Cambridge: Cambridge Univ. Press)
Gaia Collaboration, Brown, A. G. A., Vallenari, A., et al. 2016, A&A, 595, 2
Gaia Collaboration, Brown, A. G. A., Vallenari, A., et al. 2018, arXiv:1804.09365
Geng, Z. J. 2008, MsD thesis, Univ. Beijing Jiaotong
Ghosh, P., & Lamb, F. 1978, ApJL, 223, L83
Gomez, S., Mason, P. A., & Robinson, E. L. 2015, ApJ, 809, 9
Hamilton, R. T., Urban, J. A., Sion, E. M., et al. 2007, ApJ, 667, 1139
Hellier, C., Mason, K. O., Smale, A. P., et al. 1989, MNRAS, 238, 1107
Howell, S. B., Sobeck, C., Haas, M., et al. 2014, PASP, 126, 398
Ishioka, R., Kato, T., Uemura, M., et al. 2001, PASJ, 53, 905
Kato, T., Imada, A., Uemura, M., et al. 2009, PASJ, 61, 395
Kato, T., Uemura, M., Kiyota, S., et al. 2003, PASJ, 55, 489
Kennedy, M. R., Callanan, P., Garnavich, P. M., et al. 2016, AJ, 152, 27
Kepler, S. O., Kleinman, S. J., Nitta, A., et al. 2007, MNRAS, 375, 1315
Khruzina, T. S. 2011, ARep, 55, 425
Kirbiyik, H. 1982, MNRAS, 200, 907
Kjurkchieva, D., Khruzina, T., Dimitrov, D., et al. 2015, A&A, 584, 40
Knigge, C. 2006, MNRAS, 373, 484
Knigge, C., Baraffe, I., & Patterson, J. 2011, ApJS, 194, 28
Korotkiy, S. A., & Sokolovsky, K. V. 2012, ATel, 3893, 1
Krzeminski, W. 1965, ApJ, 142, 1051
Lasota, J. P. 2001, NewAR, 45, 449
Linnell, A. P., DeStefano, P., & Hubeny, I. 2012, PASP, 124, 885
Littlefair, S. P., Dhillon, V. S., Gänsicke, B. T., et al. 2014, MNRAS, 443, 718
Lomb, N. 1976, Ap&SS, 39, 447
Luri, X., Brown, A. G. A., Sarro, L. M., et al. 2018, arXiv:1804.09376
Marsh, T. R. 1999, ASPC, 160, 3
Masi, G. 2012, vsnet-alert, 14171, http://ooruri.kusastro.kyoto-u.ac.jp/mailarchive/vsnet-alert/14171
Mateo, M., Szkody, P., & Bolte, M. 1985, PASP, 97, 45
McAllister, M. J., Littlefair, S. P., Baraffe, I., et al. 2015, MNRAS, 451, 114
Mennickent, R. E., Sterken, C., Gieren, W., & Unda, E. 1999, A&A, 352, 239

Nelder, J. A., & Mead, R. A. 1965, CompJ, 308, 313
O'Connell, D. J. K 1932, BHarO, 890, 18
Ohshima, T. 2012, vsnet-alert, 14175, http://ooruri.kusastro.kyoto-u.ac.jp/mailarchive/vsnet-alert/14175
Orosz, J. A., & Hauschildt, P. H. 2000, A&A, 364, 265
Orosz, J. A., & Wade, R. A. 2003, ApJ, 593, 1032
Osaki, Y., & Kato, T. 2013a, PASJ, 65, 50
Osaki, Y., & Kato, T. 2013b, PASJ, 65, 95
Osaki, Y., & Kato, T. 2014, PASJ, 66, 15
Pala, A. F., Gänsicke, B. T., Townsley, D., et al. 2017, MNRAS, 466, 2855
Patterson, J. 1984, ApJS, 54, 443
Patterson, J. 2005, PASP, 117, 1204
Patterson, J., Thorstensen, J. R., Kemp, J., et al. 2003, PASP, 115, 1308
Pringle, J. E. 1991, ARA&A, 19, 137
Pringle, J. E., & Rees, M. J. 1972, A&A, 21, 1
Provencal, J. L., Shipman, H. L., Høog, E., & Thejll, P. 1998, ApJ, 494, 759
Prša, A., Conroy, K. E., Horvat, M., et al. 2016, ApJS, 227, 29
Qian, S. B., Han, Z. T., Fernández-Lajús, E., et al. 2015, ApJS, 221, 17
Ratti, E. M., van Grunsven, T. F. J., Jonker, P. G., et al. 2013, MNRAS, 428, 3543
Ritter, H., & Burkert, A. 1986, A&A, 158, 161
Ritter, H., & Kolb, U. 2003, A&A, 404, 301
Rutkowski, A., Waniak, W., Preston, G., & Pych, W. 2016, MNRAS, 463, 3290
Scargle, J. D. 1982, ApJ, 263, 835
Shafter, A. W. 1983, PhD thesis, Univ. California
Shafter, A. W., & Szkody, P. 1984, ApJ, 276, 305
Sion, E. M. 1999, PASP, 111, 532
Smak, J. 1970, AcA, 20, 311
Smak, J. 1994, AcA, 44, 45
Smith, D. A., & Dhillon, V. S. 1998, MNRAS, 301, 767
Stellingwerf, R. F. 1978, ApJ, 224, 953
Still, M., & Barclay, T. 2012, PyKE: Reduction and analysis of Kepler Simple Aperture Photometry data, Astrophysics Source Code Library, ascl:1208.004
Szkody, P. 1985, AJ, 90, 1837
Szkody, P., Mukadam, A. S., Odette, T., et al. 2017, AJ, 153, 123
Tody, D. 1986, Proc. SPIE, 627, 733
Tody, D. 1993, ASPC, 52, 173
Torczon, V. 1989, PhD thesis, Univ. Rice
Urban, J. A., & Sion, E. M. 2006, ApJ, 642, 1029
Wade, R. A., & Hubeny, I. 1998, ApJ, 509, 350
Warner, B. 2003, Cataclysmic Variables (Cambridge: Cambridge Univ. Press)
White, N. E., & Stella, L. 1988, MNRAS, 231, 325
Wood, J. H., & Crawford, C. S. 1986, MNRAS, 222, 645
Wood, J. H., & Horne, K. 1990, MNRAS, 242, 606
Wood, J. H., Horne, K., Berriman, G., & Wade, R. A. 1989, ApJ, 341, 974
Zorotovic, M., Schreiber, M. R., & Gänsicke, B. T. 2011, A&A, 536, 42